利用電場變調紅外線吸收光譜研究化學平衡：從簡單的液體系統到複雜的油包水乳液

學生：李依純　　指導教授：重藤真介 博士

國立交通大學分子科學研究所碩士班

摘　　要

這篇論文主要是利用電場變調紅外線吸收光譜偵測兩種凝態系統的化學平衡，針對1,2-二溴乙烷以及反微胞系統中的水兩種系統分別進行研究。第一個主題是研究 1, 2-二溴乙烷間扭式/反式間異構化平衡的反應，藉由得到的熱力學參數，可求得室溫下的平衡常數 K^0 為 0.33 (±0.04)，所以反應是趨向反式異構物；接著利用已知的熱焓差 ΔH，可以得到兩種異構物間互相轉換的吉布斯自由能差 ΔG 和熵差 ΔS，分別是 4.5 (±0.3) kJ mol^{-1} and −2.7 J K^{-1} mol^{-1}。第二部分主題是研究以界面活性劑(磺化琥珀酸二辛酯鈉)與水所組成的反微胞系統，探討水分子中羥基伸縮模式的電場變調紅外線吸收光譜。從光譜的結果得知，加電場後吸收光譜的變化，呈現一正一負兩種不同性質的圖形。且羥基伸縮模式的吸收光譜可以利用三個不同的高斯分佈曲線加以擬合，這三種分佈曲線的特性代表水分子在反微胞中大致具有三種不同的氫鍵環境，所以經由電場變調紅外線吸收光譜可以偵測不同型態水分子在反微胞內的分佈情形。

Chemical Equilibria Studied by Infrared Electroabsorption Spectroscopy: From a Simple Liquid to a Complex Water/Oil Suspension

Student：I-Chun Lee Advisor：Dr. Shinsuke Shigeto

Institute of Molecular Science

National Chiao Tung University

Abstract

Infrared (IR) electroabsorption spectroscopy is used to study chemical equilibria of the two condensed-phase systems: liquid 1,2-dibromoethane and water in reverse micelles. First, we report on experimental determination of thermodynamic parameters associated with the gauche/trans conformational equilibrium of liquid 1,2-dibromoethane. The equilibrium constant K^0 at room temperature was determined to be 0.33 (±0.04), which indicates that the trans conformer is energetically more favored than the gauche conformer. With the reported value of the enthalpy difference ΔH, we obtained the Gibbs free energy difference ΔG and the entropy difference ΔS between the two conformers as 4.5 (±0.3) kJ mol^{-1} and −2.7 J K^{-1} mol^{-1}, respectively. In the second system, we measured IR electroabsorption spectra in the OH stretching region of water in aerosol OT reverse micelles. The observed IR electroabsorption spectrum shows a bipolar feature with intensity moving from the red to the blue. The OH stretching absorption band is deconvoluted to three

Gaussian subbands, which correspond to distinct hydrogen-bonding environments. The IR electroabsorption spectrum may be interpreted in terms of a field-induced population change among those three kinds of water molecules, which are assumed to occur in equilibrium.

Acknowledgements

兩年匆匆過去了，碩士生涯正式畫上句點。這段時間，要感謝很多人的幫忙和鼓勵，所以我才能順利地完成研究。首先，我想要感謝指導教授重藤真介，給予我良好的學習及實驗環境，讓我了解到做實驗時應該保持嚴謹且正面的態度，學習要把所有事情做到盡善盡美。再者，感謝日本東京大學濵口宏夫教授，會時常安排時間和機會來台灣給予許多指教，使我從中學習並且獲益良多。感謝實驗室的成員，藪本宗士博士、傳耿學長、Hemanth Nag 學長、Sudhakar Narra 學長、威威學弟和齡云助理，在實驗以及研究過程中給予指導和幫助。在此也特別感謝交通大學張豐志教授和鄭智嘉學長協助在 DLS 上的量測，讓我可以順利完成我的碩士學位。

感謝廖奕翰教授實驗室的小蔥、sheep、嘉仁學弟、士豪學弟、Jessica 學妹、大衛學弟，總是會聽我碎碎唸和幫忙我處理一些雜事。感謝孫建文教授實驗室的育麟學長、昭凱學長、老柯學長、子漢學長、宗儀學長、KB 學長、政元、柏帆、老*、龍五、靜宜學妹、麵包學妹，和大家一起出遊、烤肉的時光總是很快樂，我會一直記住的。感謝我的高中同學兔子、蕃茄、嚕嚕米，很慶幸地大家都在新竹唸碩班，能時常一起出去吃飯、聊天。感謝明諺學長，總是陪我練桌球且又得接收我的低氣壓，還得不停地講道理給我聽。感謝我的好朋友趙屁、丸子、婉茜、北七胡，在我沮喪或是實驗不順時，不停地替我打氣，相信我可以做到。

最後，我要感謝最疼愛我的老爸和老媽，兩年期間，給予我經濟上的支柱，讓我可以在國立交通大學順利地學習與成長。並且總是給予我鼓勵和支持，讓我能有往前的力量，謝謝你們。

Table of Contents

List of Figures and Tables

Chapter I

Introduction

Electrostatic interaction of molecules plays a central role in chemistry. In a liquid or a solution, a molecule is continuously exposed to the electrostatic interaction (the dipolar or dispersion interaction) among the surrounding molecules, which may influence the direction and rate of chemical reactions. Stark spectroscopy is a powerful method for probing electrostatic interactions of molecules exposed to an externally applied electric field. The Stark effect refers to the effect of an applied electric field on an absorption or emission spectrum. The terms electroabsorption, electro-optic absorption, and electrochromism have also been used in the literature to describe the same phenomenon.

Stark spectroscopy provides unique information on molecular properties in diverse systems ranging from isolated gas-phase molecules to complex biological systems. There has been a number of studies using electroabsorption [1-4]. In particular the Stark effect in the visible region has been extensively studied. A series of pioneering work was conducted by Liptay and co-workers [5, 6]. Not only did Liptay demonstrate experimental determination of electric properties of many simple aromatic solutes in solutions [5], but laid down a theoretical basis of Stark spectroscopy [6], which is now generally used in this area. By working with frozen glasses, Boxer and co-workers enabled Stark spectroscopic studies of molecular systems such as donor–acceptor polyenes and transition metal complexes (metal-to-ligand and metal-to-metal mixed valence transitions) and nonphotosynthetic biological systems [1, 7]. They quantitatively discussed the amount of charge transfer based upon two characteristic parameters obtained directly from experiment: the change in dipole moment, $\Delta\mu$, and the change in polarizability, $\Delta\alpha$, between the ground and excited *electronic* states. Ohta and co-workers [2, 8-11] examined the electric-field effects on absorption and fluorescence spectra of polymer films with specific dopant molecules. In one of their recent studies, they obtained $\Delta\mu$ and $\Delta\alpha$ of the two different dopants (2-hydroxyquinoline or 6-hydroxyquinoline) embedded in a polymer film through

temperature dependence and polarization dependence [8, 9]. Those parameters are important and useful for developing and designing novel photonic devices.

Since vibrational spectra are sensitive to molecular structures, one expects that electroabsorption in the mid-infrared (mid-IR) is an excellent tool for studying the Stark effect in relation to structural properties of molecules. As early as 1967, for instance, Handler and Aspnes [12] did use IR electroabsorption spectroscopy to study the Stark effect on the O–H stretching mode of 2,6-diisopropyl phenol in CCl_4 and obtained the parameters associated with the dipole moment and the polarizability of the alcohol. However, mainly due to technical difficulties, there were much fewer studies of electroabsorption spectroscopy in the infrared in comparison to those in the visible.

In 1995, Chattopadhyay and Boxer [13] reported the use of vibrational Stark spectroscopy to study the electric-field effect on the CN stretching mode of anisonitrile in toluene at 77 K. They evaluated $\Delta\mu$ and $\Delta\alpha$ between the *vibrational* states involved. The Boxer group extended their research to a series of compounds that contain the CN group [14]. In 2002 [15], they applied the technique to free CO and CO bound to myoglobin (Mb). It is shown that the change in dipole moment for the CO bound to Mb is larger than that for the free CO because of $d-\pi^*$ back-bonding. More recently, they used the shift of the CN stretching frequency to probe electrostatic fields in even more complex biological systems such as a protein and the active site of an enzyme [4, 16].

These studies have all been performed at the liquid-nitrogen temperature (77 K), where orientational motion of molecules is literally frozen or suppressed to a great extent. Working at low temperatures makes interpretation of the Stark spectra simpler, because the electronic response via $\Delta\mu$ and $\Delta\alpha$ is the only dominant contribution. Those spectra, however, lack in the information on the orientational response to an applied field, which is very useful for understanding molecular structures and association in liquids and solutions.

Hiramatsu and Hamaguchi developed an electroabsorption apparatus that was intended for mid-IR, room-temperature measurements [3]. Using a dispersive IR spectrometer equipped with an AC-coupled amplifier rather than using the FT-IR method, they were able to detect IR absorbance changes as small as 10^{-7}. Hamaguchi and co-workers first used their unique method to investigate the trans/gauche conformational equilibrium of liquid 1,2-dichloroethane (DCE) [17], followed by the studies of the self-association of *N*-methylacetamide in 1,4-dioxane [18], association forms of liquid crystal (5CB) [19], and solvated structures of *p*-nitroaniline (pNA) in acetonitrile/CCl_4 [20]. In 2007 the whole setup was transferred and reconstructed here by us. In the present work, the author utilizes infrared electroabsorption spectroscopy to study the trans/gauche conformational equilibrium and associated thermodynamic parameters of liquid 1,2-dibromoethane (DBE) and water in AOT reverse micelles (RMs).

The rest of this dissertation is organized as follows. In Chapter II, the theoretical background of IR electroabsorption spectroscopy is outlined. Three major contributions to observed absorbance changes are considered. Chapter III describes the details of IR electroabsorption apparatus and the sample cell used. In Chapter IV, the application to the trans/gauche conformational equilibrium of liquid DBE is presented. The Gibbs free energy difference ΔG and entropy difference ΔS, of the trans/gauche equilibrium of liquid DBE have been experimentally determined for the first time [21]. We compare the results with those of DCE [17] and discuss intermolecular interaction in liquids DBE and DCE. Chapter V deals with IR electroabsorption of water in reverse micelles. We observed the electroabsorption spectrum of the O-H stretching band of water in RMs. It is likely that the spectrum is well accounted for by assuming the change in equilibrium population of three subbands within the O-H stretching band. Chapter VI is devoted to concluding remarks.

Chapter II

Theoretical Background

In this chapter, the theoretical basis of infrared electroabsorption spectroscopy is described. The formulation of several molecular responses to an external electric field modulation is given. Some of the equations derived here will be used in the following chapters to analyze observed IR electroabsorption spectra.

II-1. Infrared Electroabsorption Spectroscopy

When an electric field is applied to the system, an absorbance change (ΔA) is induced. The absorbance change ΔA is calculated from the intensity change ΔI as follows:

$$\begin{aligned}\Delta A &= A_{\text{on}} - A_{\text{off}} \\ &= \left\{-\log\left(\frac{I_{\text{on}}}{I_0}\right)\right\} - \left\{-\log\left(\frac{I_{\text{off}}}{I_0}\right)\right\} \\ &= -\log\left(1+\frac{\Delta I}{I}\right)\end{aligned} \tag{II-1}$$

Here I_0 represents the intensity of the IR light (reference signal), I ($=I_{\text{off}}$) the intensity of the IR light that transmit the sample without being applied the electric field, and ΔI the difference, $I_{\text{on}} - I_{\text{off}}$, between the intensities measured with and without the electric field.

The absorbance change can be expanded in a power series of the electric field of the form $F(t) = F_0 \sin(2\pi f t)$:

$$\Delta A(\tilde{\nu}; F_0) = \Delta A(\tilde{\nu}; F_0^2, 2f) + \Delta A(\tilde{\nu}; F_0^4, 4f) + \Delta A(\tilde{\nu}; F_0^6, 6f) + \cdots . \tag{II-2}$$

Since $F(t)$ and $F(t + 1/2f)$ give the same absorbance change, only the even-order terms are to be observed. In our experiments, the lowest-order term is selectively probed with a lock-in voltmeter; they are thus viewed as the second-order Stark spectroscopy.

II-2. Three Types of Signals

An absorbance change (ΔA) originates from different molecular responses to an applied electric field. There are three important molecular responses to be considered in this work: orientational polarization, electronic polarization, and equilibrium change [3]. In the following, we derive the expression of the ΔA signal for each of the responses and see how

they contribute to the ΔA spectrum.

II-2-1. Orientational Polarization Signal

Consider a sample in which molecules having a permanent dipole moment $\boldsymbol{\mu}_p$ distribute over the space with random orientation. Upon application of an external electric field to the sample, the dipoles tend to be aligned along the direction of the applied electric field. Orientational anisotropy so induced contributes to the change in absorption spectrum of the sample.

Case 1: Normally Incident Nonpolarized Light

To derive the expressions for the orientational polarization ΔA signal, let us begin by Beer-Lambert law:

$$\begin{aligned} A &= \varepsilon c \ell \\ &= c\ell \cdot K\tilde{\nu} \int_0^{\pi} \sin\theta \, \mathrm{d}\theta \cdot f(\theta) \cdot \frac{1}{2\pi}\int_0^{2\pi} \mathrm{d}\varphi \times \frac{1}{2\pi}\int_0^{2\pi} \mathrm{d}\psi \, (\boldsymbol{e}\cdot\boldsymbol{\mu}_T)^2 \end{aligned} \tag{II-3}$$

where ε is the molar extinction coefficient, c the sample concentration (mol dm^{-3}), ℓ the pass length (cm) of the sample, K a proportionality constant, $\tilde{\nu}$ the wavenumber (cm^{-1}), and e a unit vector designating the direction of the electric field of the incident light. In Figs. II-1 and II-2, we set the molecule-fixed coordinate system such that the z-axis coincides with the direction of the applied electric field and the propagation direction of the IR light. The orientations of the dipole moment $\boldsymbol{\mu}_p$ and of the transition moment $\boldsymbol{\mu}_T$ are determined by the angles θ, ϕ, and φ. In Eq. II-3, there are two integrands to be obtained explicitly; one is a spatial distribution function $f(\theta)$, and the other is the square of the scalar product of the transition moment and the unit vector, $(\boldsymbol{e}\cdot\boldsymbol{\mu}_T)^2$.

The distribution function $f(\theta)$ is proportional to the probability of the dipole moment $\boldsymbol{\mu}_p$ to be found in the direction θ with respect to the applied electric field $\boldsymbol{F}$. Using the coordinate system shown in Figs. II-1 and II-2, we have

$$\boldsymbol{\mu}_{\mathbf{p}} = \mu_p \begin{pmatrix} \sin\theta\ \cos\phi \\ \sin\theta\ \sin\phi \\ \cos\theta \end{pmatrix},\ \boldsymbol{F} = F \begin{pmatrix} 0 \\ 0 \\ 1 \end{pmatrix},\ \mathbf{e} = e \begin{pmatrix} \cos\psi \\ \sin\psi \\ 0 \end{pmatrix} \tag{II-4}$$

The number of molecules that have energy E is proportional to $\exp\left(-\frac{E}{k_{\mathrm{B}}T}\right)$, and the energy E due to the dipolar interaction is given by

$$E = -\boldsymbol{\mu}_{\mathrm{p}} \cdot \boldsymbol{F} = -\mu_{\mathrm{p}} \begin{pmatrix} \sin\theta\cos\varphi \\ \sin\theta\sin\varphi \\ \cos\theta \end{pmatrix}^{\mathrm{T}} \cdot F \begin{pmatrix} 0 \\ 0 \\ 1 \end{pmatrix} = -\mu_{\mathrm{p}} F\ \cos\theta \tag{II-5}$$

Thus the distribution function $f(\theta)$ becomes

$$f(\theta) = \mathrm{C} \cdot \exp\left(\frac{\mu_p F\ \cos\theta}{k_{\mathrm{B}}T}\right) = \mathrm{C} \cdot \exp(\gamma\cos\theta) \tag{II-6}$$

with

$$\gamma = \frac{\mu_p F}{k_{\mathrm{B}}T}. \tag{II-7}$$

Here C is a normalization factor, T is the temperature, k_{B} is the Boltzmann constant, and F is the internal (not external) field strength. The parameter γ reflects the extent of the electrostatic interaction and plays a central role throughout this thesis. The normalization factor C is determined by the condition

$$\int_0^{2\pi}\int_0^{\pi} f^{\mathbf{on}}(\theta)\sin\theta d\theta d\phi = 1 \tag{II-8}$$

In the presence of the electric field ($F \neq 0$), $f(\theta)$ becomes from Eqs. II-6 and II-8

$$f^{\mathrm{on}}(\theta) = \frac{1}{2\pi}\frac{\gamma}{\exp(\gamma)-\exp(-\gamma)} \cdot \exp(\gamma\cos\theta) \tag{II-9}$$

In the absence of the electric field $(F = 0)$, we obtain $f(\theta)$ by taking the $\gamma \to 0$ limit of Eq. II-9

$$f^{\mathrm{off}}(\theta) = \frac{1}{4\pi} \tag{II-10}$$

The scalar product of $\boldsymbol{\mu}_T$ and e can be calculated as follows. The electric field vector $\boldsymbol{e}$, of the incident light lies in the xy-plane, and a projection of $\boldsymbol{\mu}_T$ onto the xy-plane is related to $(\mu_T \cdot e)^2$. $\boldsymbol{\mu}_T$ is expressed as

$$\boldsymbol{\mu_T} = |\mu_T| \cdot \begin{pmatrix} -\cos\varphi\cos\theta\cos\phi\sin\alpha - \sin\varphi\sin\phi\sin\alpha + \cos\varphi\sin\theta\cos\alpha \\ -\sin\varphi\cos\theta\cos\phi\sin\alpha + \cos\varphi\sin\phi\sin\alpha + \sin\varphi\sin\theta\cos\alpha \\ \sin\theta\cos\phi\sin\alpha + \cos\theta\cos\alpha \end{pmatrix} \tag{II-11}$$

If $\boldsymbol{\mu}_p$ is parallel to μ_T, i.e., $\alpha = 0°$ as shown in Fig. II-1, Eq. II-11 is reduced to

$$\boldsymbol{\mu_T} = \mu_T \cdot \begin{pmatrix} \sin\theta\cos\varphi \\ \sin\theta\sin\varphi \\ \cos\theta \end{pmatrix} \tag{II-12}$$

With use of Eqs. II-4 and II-12, $(\mu_T \cdot e)^2$ is obtained as

$$(\mu_T \cdot e)^2 = \frac{1}{2}\mu_T^2 \sin^2\theta \tag{II-13}$$

Here we replace $\cos^2\psi$, $\sin^2\psi$, and $\cos\psi\ \sin\psi$ by their mean values for $0 \le \psi \le 2\pi$ (1/2, 1/2, and 1, respectively). In the absence of the external electric field, the absorbance A^{off} for an $\alpha = 0^\circ$ vibrational mode is calculated from Eqs. II-3, II-10 and II-13 as

$$\begin{aligned} A^{\text{off}} &\propto \int_0^{2\pi}\int_0^{\pi} f^{\text{off}}(\theta) \cdot \sin\theta \cdot \left|e \cdot \boldsymbol{\mu_T}\right|^2 d\theta d\varphi \\ &= \frac{1}{4\pi} \cdot \frac{1}{2}\mu_T^2 \int_0^{2\pi}\int_0^{\pi} \sin^3\theta \cdot d\theta d\varphi \\ &= \frac{1}{3}\mu_T^2 \end{aligned} \tag{II-14}$$

Similarly, substitution of Eqs. II-9 and II-13 into Eq. II-3 results in the absorbance for the $\alpha = 0^\circ$ mode when the electric field is turned on

$$\begin{aligned} A^{\text{on}} &\propto \int_0^{2\pi}\int_0^{\pi} f^{\text{on}}(\theta) \cdot \sin\theta \cdot \left|e \cdot \boldsymbol{\mu_T}\right|^2 d\theta d\varphi \\ &= \frac{1}{2}\mu_T^2 \cdot \frac{\gamma}{(e^{\gamma} - e^{-\gamma})} \cdot \left[\frac{2}{\gamma^2}(e^{\gamma} + e^{-\gamma}) - \frac{2}{\gamma^3}(e^{\gamma} - e^{-\gamma})\right] \end{aligned} \tag{II-15}$$

By developing the exponential functions and retaining terms up to third-order in γ, we have

$$A^{\text{on}} \propto \frac{2}{\gamma^2 + 6} \cdot \mu_{\text{T}}{}^2 \tag{II-16}$$

As will be shown later, the assumption made here ($\gamma << 1$) is valid in our experiments. The absorbance change caused by the applied electric field is the difference between A^{on} (Eq. II-16) and A^{off} (Eq. II-15). The absorbance change ratio is thus

$$\frac{\Delta A}{A^{\text{off}}} = \frac{A^{\text{on}} - A^{\text{off}}}{A^{\text{off}}} = -\frac{\gamma^2}{\gamma^2 + 6} \tag{II-17}$$

Next we consider the $\alpha = 90^{\text{o}}$ case where $\boldsymbol{\mu}_{\mathbf{p}}$ is perpendicular to μ_{T} (Fig. II-2). Equation II-11 reduces to

$$\boldsymbol{\mu}_{\boldsymbol{T}} = \mu_T \cdot \begin{pmatrix} -\cos\varphi\,\cos\theta\,\cos\phi - \sin\varphi\,\sin\phi \\ -\sin\varphi\,\cos\theta\,\cos\phi + \sin\varphi\,\cos\phi \\ \cos\phi\,\sin\theta \end{pmatrix} \tag{II-18}$$

and $(\mu_{\text{T}} \cdot \text{e})^2$ yields

$$(\mu_{\text{T}} \cdot \text{e})^2 = \frac{1}{4}\mu_T{}^2(\cos^2\theta + 1) \tag{II-19}$$

Making use of Eqs. II-3, II-9, II-10 and II-19, we end up with the absorbance change ratio of the form

$$\frac{\Delta A}{A^{\text{off}}} = \frac{\gamma^2}{2(\gamma^2 + 6)} \tag{II-20}$$

Generalization of Eqs. II-17 and 20 to an arbitrary angle α is straightforward. The absorbance change for angle α can be decomposed into its parallel $(\alpha = 0^{\text{o}})$ and perpendicular $(\alpha = 90^{\text{o}})$ components as follows:

$$\Delta A_\alpha = \left(\frac{\Delta A}{A}\right)_{\parallel} \left|\mu_T \cos\alpha\right|^2 + \left(\frac{\Delta A}{A}\right)_{\perp} \left|\mu_T \sin\alpha\right|^2 \tag{II-21}$$

Substitution of Eqs. II-17 and II-20 yields the following expression for the orientational polarization signal probed with the normal incidence

$$\Delta A_{\alpha} = \frac{\gamma^2}{2(\gamma^2 + 6)}\left(1 - 3\cos^2\alpha\right) \cdot A \qquad \text{(II-22)}$$

Again γ^2 is exceedingly smaller than 6 in the present study, so the first term in the denominator of Eq. II-22 is safely neglected. Therefore we are left with

$$\frac{\Delta A_{\alpha}}{A} = \frac{\gamma^2}{12}\left(1 - 3\cos^2\alpha\right) \qquad \text{(II-23)}$$

Case 2: p-Polarized Light with Tilted Incidence

So far we have considered the case where the electric field vector of the incident, nonpolarized light on the *xy*-plane is parallel to the sample cell. In other words, χ is equal to 90°, where χ is the angle between the applied electric field ***F*** and the electric-field vector ***e*** of the incoming IR light (see Fig. II-3). When p-polarized light whose electric field vector ***e*** has only *x*-component is incident upon the sample with angle χ, the absorbance change ratio is given by

$$\frac{\Delta A_{\alpha,\chi}}{A} = \frac{1}{12}\left(\frac{\mu_p F}{K_B T}\right)^2 \left(1 - 3\cos^2\alpha\right)\left(1 - 3\cos^2\chi\right), \qquad \text{(II-24)}$$

It should be noted that $\Delta A_{\alpha,\chi} / A$ shows the $1 - 3\cos^2\chi$ dependence and that the signal disappears if $\chi = 54.7°$. Another important point is that the orientational polarization ΔA spectrum is proportional to the absorption spectrum *A*, indicating that it is manifested as the zeroth derivative shape of the absorption spectrum.

II-2-2. Electronic Polarization Signal

An absorbance change also arises from the electronic polarization signal, which is the change by an externally applied field in molecule's electronic properties such as the dipole moment and the polarizability. A general theory that describes the electronic polarization signal was established by Liptay and co-workers [5, 6]. For a molecule in solution, the electronic polarization signal is given by the following formula [22, 23]

$$\Delta A(\tilde{\nu}) = F^2 \left[A_\chi A(\tilde{\nu}) + \frac{B_\chi}{15h} \tilde{\nu} \frac{\mathrm{d}}{\mathrm{d}\tilde{\nu}} \frac{A(\tilde{\nu})}{\tilde{\nu}} + \frac{\mathrm{C}_\chi}{30h^2} \tilde{\nu} \frac{\mathrm{d}^2}{\mathrm{d}\tilde{\nu}^2} \frac{A(\tilde{\nu})}{\tilde{\nu}} \right] \tag{II-25}$$

This equation consists of the zeroth, first, and second derivatives of the absorption band. The coefficients A_χ, B_χ and C_χ are

$$A_\chi = \left(3\cos^2\chi - 1\right) \left[\frac{\mu_\mathrm{g}^2}{30k_\mathrm{B}^2T^2} \left(3\hat{\mathrm{m}}^2 - 1\right) + \frac{1}{10k_\mathrm{B}T} \left(\alpha_\mathrm{gm} - \frac{1}{3}\Delta\alpha_\mathrm{g} \right) \right] \tag{II-26}$$

$$\begin{aligned} B_\chi = {} & \frac{5}{k_\mathrm{B}T} \left(\mu_\mathrm{g} \cdot \Delta\mu\right) + \frac{5}{2} \mathrm{Tr}\,\Delta\alpha \\ & + \left(3\cos^2\chi - 1\right) \left[\frac{1}{kT} \left(\mu_\mathrm{g} \cdot \Delta\mu\right) \left(3\hat{\mathrm{m}}^2 - 1\right) + \left(\frac{3}{2}\Delta\alpha_\mathrm{m} - \frac{1}{2}\mathrm{Tr}\,\Delta\alpha \right) \right] \end{aligned} \tag{II-27}$$

$$\mathrm{C}_\chi = 5\left|\Delta\mu\right|^2 + \left|\Delta\mu\right|^2 \left(3\cos^2\chi - 1\right)\left(3\hat{\mathrm{m}}^2 - 1\right) \tag{II-28}$$

where *c* is the speed of light, and *h* is Planck's constant. $\Delta\mu$ and $\Delta\alpha$ denote the change in permanent dipole moment and polarizability tensor between vibrational ground state (g) and excited state (e), respectively. $\hat{\mathrm{m}}$ is a unit vector in the direction of the transition dipole moment. α_gm and $\Delta\alpha_\mathrm{m}$ are the components of the polarizability change along the direction of the transition dipole moment, i.e., $\alpha_\mathrm{gm} = \hat{\mathrm{m}} \cdot \alpha_\mathrm{g} \cdot \hat{\mathrm{m}}$ and $\Delta\alpha_\mathrm{m} = \hat{\mathrm{m}} \cdot \Delta\alpha \cdot \hat{\mathrm{m}}$. The changes in dipole moment and polarizability upon vibrational excitation are in general very small, because the vibrational states involved belong to the same electronic state. So the electronic polarization signal in IR electroabsorption is small too.

The zeroth-derivative component represents *the intensity change* of an absorption spectrum. Note that the first term in the square brackets in Eq. II-26 corresponds to the orientational polarization contribution, which we already derived above. The first-derivative component depends on both $\Delta\mu$ and $\Delta\alpha$, and is responsible for *the peak shift*, as illustrated in Fig. II-4. The second-derivative component, which is characterized by $\Delta\mu$, shows *the change of the bandwidth* of the absorption spectrum (see Fig. II-5).

II-2-3. Equilibrium Change Signal

In addition to the orientational polarization and the electronic polarization signals, the ΔA signal due to an equilibrium change may be observed when more than one species coexist in equilibrium. To see the origin of this signal, let us imagine that there exist two species X and Y in equilibrium, $X \leftrightarrow Y$, and that species X interacts with an external electric field to a greater extent than species Y does. Due to larger stabilization via the electrostatic interaction with the applied field, the population of species X increases and concomitantly that of Y decreases, giving rise to an equilibrium shift towards X. Since this equilibrium change signal is a change in absorption intensity, the ΔA spectrum due to the equilibrium change has the same spectral shape as the absorption spectrum. Therefore, the equilibrium change signal contributes to the zeroth-derivative component of the ΔA signal as the orientational polarization signal does. However it is possible to differentiate those two contributions by looking at the χ dependence; the orientational polarization signal is χ dependent, whereas the equilibrium change signal is χ independent. More details of the equilibrium change signal will be given in Chapter IV, where we study the trans–gauche conformational equilibrium of liquid 1,2-dibromoethane with IR electroabsorption spectroscopy.

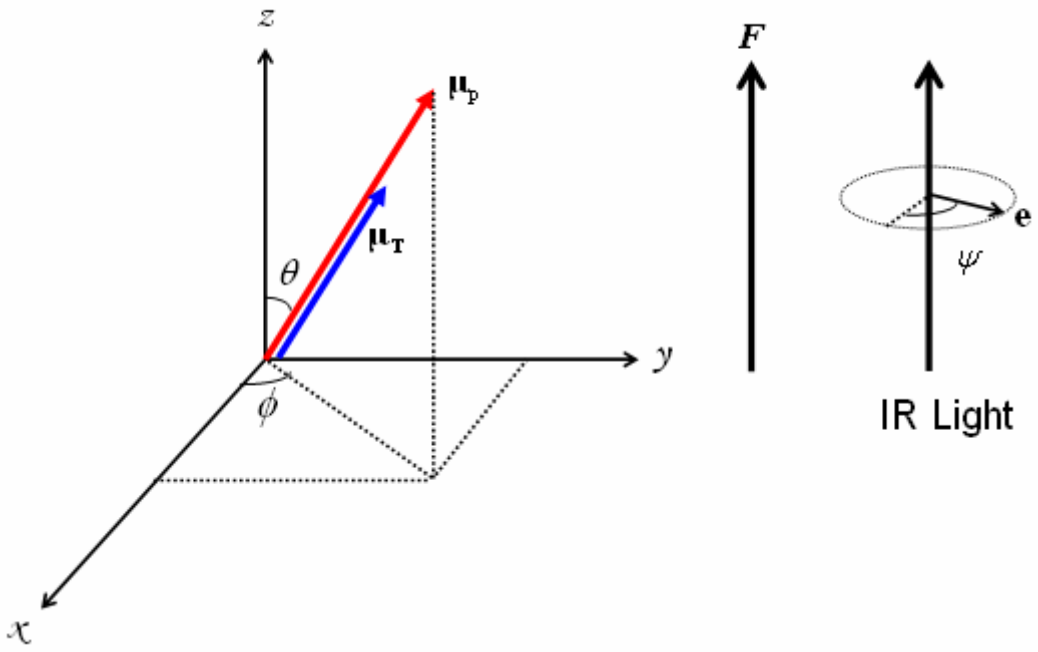

Figure II-1. Coordinates used in derivation of the orientational polarization signal. α is the angle between $\boldsymbol{\mu}_p$ and $\boldsymbol{\mu}_T$. This figure corresponds to the $\alpha = 0^o$ case where $\boldsymbol{\mu}_p$ is parallel to $\boldsymbol{\mu}_T$.

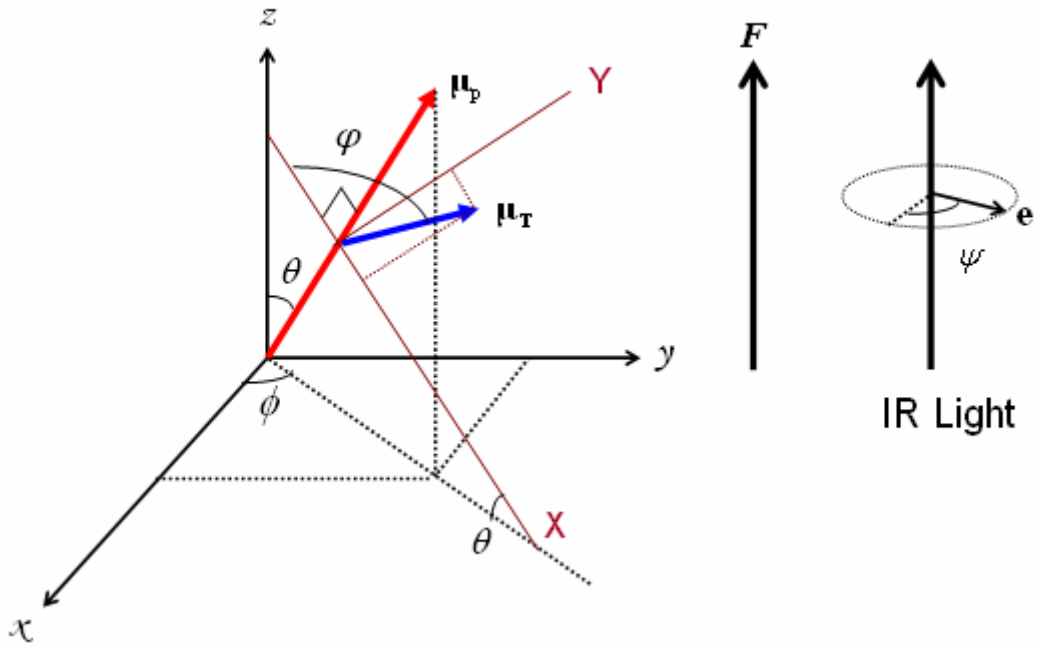

Figure II-2. Coordinates used in derivation of the orientational polarization signal. This figure corresponds to the $\alpha = 90°$ case where $\boldsymbol{\mu}_p$ is perpendicular to $\boldsymbol{\mu}_T$.

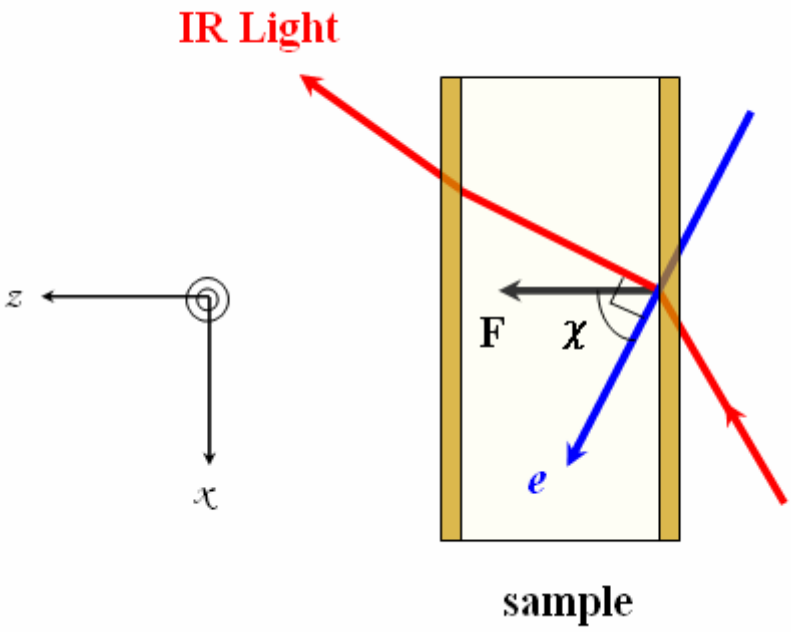

Figure II-3. Angle χ between the applied electric field ***F*** and the electric-field vector ***e*** of the incoming IR light.

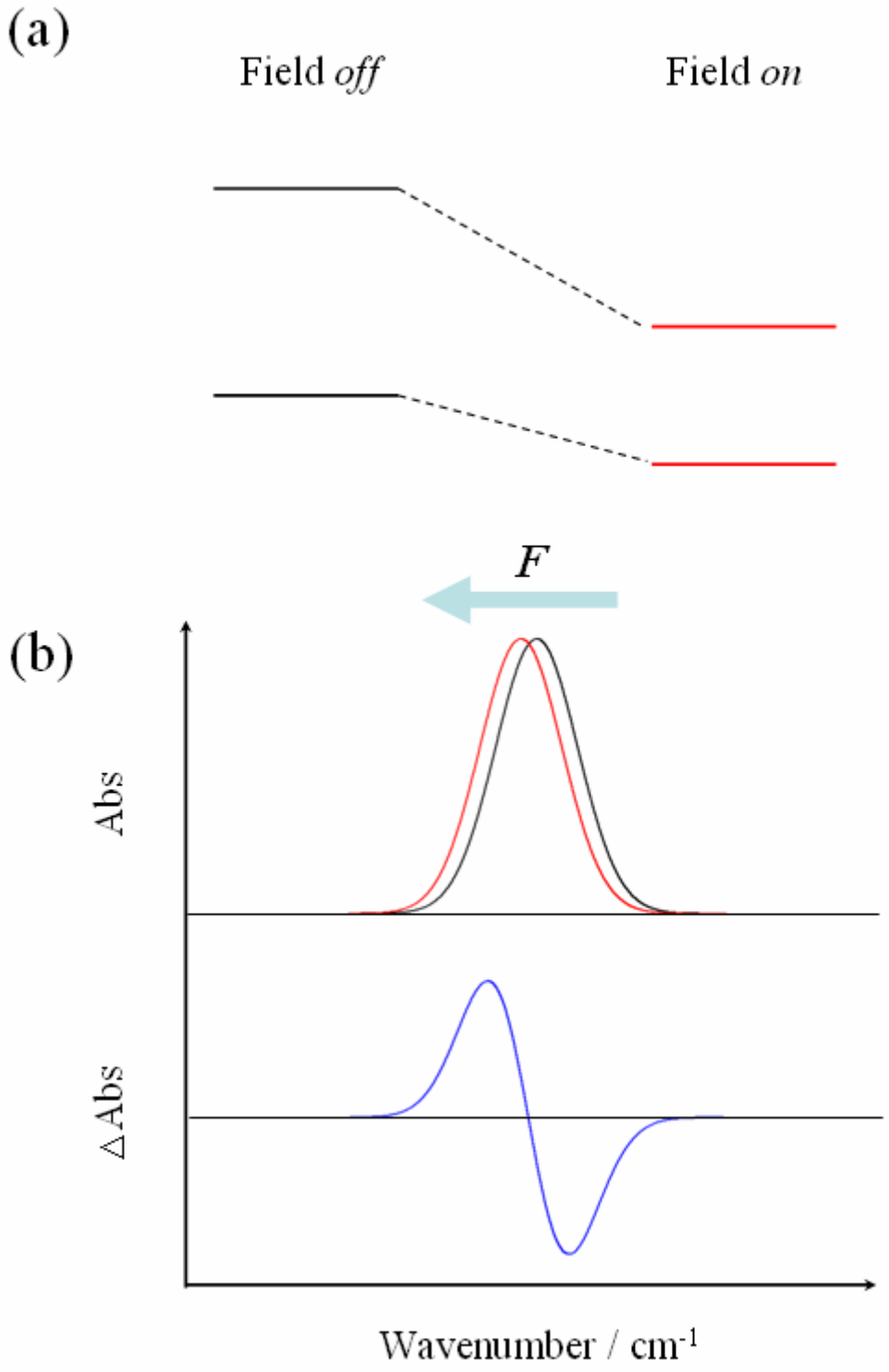

Figure II-4. (a) Electric field effect on the ground and excited states. (b) An absorption peak shifts to lower frequency ($\Delta\alpha > 0$), and the ΔA spectrum exhibits a first-derivative line shape (not to scale).

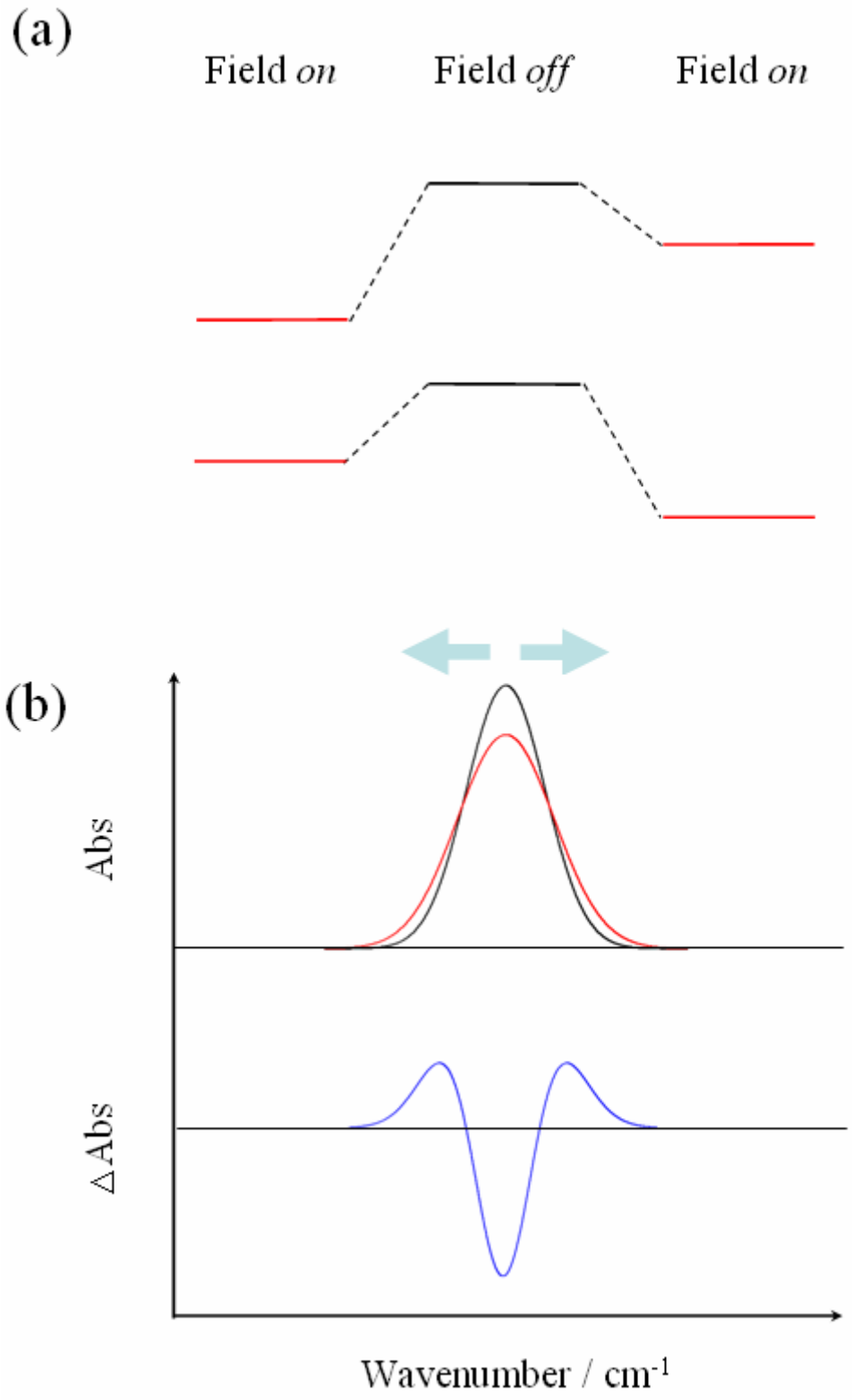

Figure II-5. (a) Electric field effect on the distribution of the transition frequency from the ground to an excited state. (b) The difference in absorbance spectrum has a second-derivative line shape (not to scale).

Chapter III

Experimental

The experimental setup of IR electroabsorption spectroscopy and the configuration of the sample cell used in the present study are introduced in this chapter. Those were originally developed by Hiramatsu and Hamaguchi [3] at the University of Tokyo. We transferred and rebuilt the whole system here with some improvements. In what follows, the characteristics of the apparatus and several technical difficulties arising in the measurements are discussed.

III-1. Experimental Setup

A schematic of our experimental setup is depicted in Fig. III-1. The system consists of a light source, a home-built sample cell, an optical chopper, a dispersive IR monochromator, a photoconductive HgCdTe (MCT) detector (New England Research Center, MPP12-2-J3) or InSb detector (Kolmar Technologies, KISDP-1-J1/DC), an AC-coupled amplifier, and a lock-in voltmeter (Standard Research Systems Inc., SR844). The light source, a ceramic mid-IR emitter, is used to illuminate the sample. The new light source used in this work can be handled easily with constant voltage setting in comparison to the previous one. As shown in Fig. III-1, the optical chopper (Stanford Research Systems Inc., SR540) and the sample cell are set at the co-focus of the ellipsoidal mirror pair and at the other focus of the second ellipsoidal mirror, respectively. The function generator (IWATSU, FG-330) and the power amplifier (NF Corporation, 4010) produce an AC voltage (25 kHz sinusoidal wave), which is applied across the sample about 5 μm thick. The dispersive mid-IR monochromotor (JASCO, TRIR-1000) in combination with AC-coupled amplification enables us to detect absorbance changes as small as $\sim 1 \times 10^{-7}$ induced by the applied electric field. The sensitivity of our spectrometer is in fact better than or at least comparable to that achieved by the latest FTIR method [24]. Note that the intensity change of the transmitted IR light we detect is proportional to E^2 and hence it appears at 50 kHz, twice the frequency of the applied electric field (see the discussion in Chapter II). The MCT detector is used for measurements in the fingerprint region and the InSb detector for those in the C–H and O–H stretch region.

In the experiment we begin by measuring the intensity of the light source itself, I_0, followed by the measurement of the intensity, I, of the IR light that passed through the sample but without an external electric field. I_0 and I are obtained using a digital sampling oscilloscope (LeCroy, LC334-DSO) and the mechanical chopper operating at about 240 Hz. We can compute from I_0 and I the absorbance A as follows:

$$A = \log\left(\frac{I_0}{I}\right) \tag{III-1}$$

Next the AC-coupled method and phase-sensitive detection (PSD) with the lock-in voltmeter are employed to detect a transmitted intensity change ΔI due to electric-field modulation. ΔI is typically of the order of 10^{-6} and is overwhelmed by the huge DC offset I. The output of the detector enters a low-noise preamplifier (NF Corporation, NF218), where only the AC component of the signal is obtained and amplified. The AC component is subject to further amplification with a main amplifier (NF Corporation, 5305) and then sent to the lock-in voltmeter in order to extract from noises the AC component whose frequency coincides with the reference signal $2f$. A computer converts the intensity change ΔI to the absorbance change ΔA:

$$\Delta A = -\log\left(1 + \frac{\Delta I}{I}\right) \tag{III-2}$$

PSD works in the following way [25, 26]. The electric-field-induced signal has the same frequency as the reference, while the noises from the surroundings have arbitrary (and sometimes random) frequencies. The lock-in amplifier receives a reference signal (square wave) which is a synchronous output derived from the function generator and produces a lock-in reference signal (sinusoidal wave) by a phase-locked loop (PLL). Meanwhile, the output signal from the main amplifier is led to the phase-sensitive detector of the lock-in amplifier, where the two signals (the amplified output signal and the phase-locked reference signal) are mixed. The product of these two input signals can be expressed as a superposition

of two sinusoidal waves with the sum and difference frequencies. This output then passes through a low-pass filter, and the sum-frequency component is removed. In contrast the difference-frequency component (a DC signal in this case) remains unaffected by the low-pass filter. In this way, the noises are removed to a great extent and the electric-field-induced signal can be selectively detected.

III-2. Sample Cell

Our home-built sample cell is worth mentioning. It was designed by Hiramatsu and Hamaguchi [3] so that they can flow the sample through it as well as apply an electric field across it. The configuration of the cell is schematically shown in Fig. III-2. It consists of a brass cell holder (A/A'), two silicon windows (B/B') 0.5 mm thick, and a polyethylene terephthalate (PET) film (C) as a spacer. The PET film (Mitsubishi Plastics, Diafoil K205-6E) must be thin enough to avoid using very high voltage. The thickness of the PET film is approximately 6 μm, but the actual cell gap was estimated every measurement by the method described below. The Si plates (Pier Optics) also serve as electrodes, because they are made of p-type boron-doped wafers having the resistivity 0.8–2 Ω cm. Using chemically durable perfluoroelastmer O-rings (As568A-008) for the holes at A' and B' prevents the sample liquid from leaking out of the flow system. To avoid sample evaporation because of heat accumulation, we kept the sample flow during the measurement.

In order to reduce a voltage discrepancy between A–A' ($V_{AA'}$) and B–B' ($V_{BB'}$), we should decrease the contact resistance between them as small as possible. We scratched the surface of the Si window at two points that are separated by ~2 cm so as to remove the oxide layer and to put Indium-Gallium alloy on those points. The resistance between the two points was measured to make sure that it was less than ~20 Ω. It depends upon the doping property of Si. A large resistance may give rise to the decrease in amplitude of the applied voltage and phase retardation with respect to the applied sinusoidal wave. The latter appears, in many

cases, as nonzero out-of-phase ΔA signals. This phenomenon has been accounted for by regarding the sample cell as forming an RC circuit [3]. Figure III-3 shows an RC circuit equivalent to the sample cell. Here R_1 and R_2 designate the resistances between A–B and A' –B', respectively, and C_c is the capacitance between the electrodes. The effective voltage across the sample ($V_{BB'}$) is related to the applied voltage ($V_{AA'}$) as [3]

$$V_{BB'} = V_{AA'} \cdot \frac{1}{\sqrt{1+(\omega RC_c)^2}} \left(\frac{1}{\sqrt{1+(\omega RC_c)^2}} + i \frac{\omega RC_c}{\sqrt{1+(\omega RC_c)^2}} \right) \quad \text{(III-3)}$$

where $R = R_1 + R_2$. The amplitude and phase retardation of the voltage $V_{BB'}$ are thus given by

$$\text{Amplitude} = \frac{V_{AA'}}{\sqrt{1+(2\pi fRC_c)^2}}, \quad \text{(III-4)}$$

$$\text{Retardation} = \phi = \arctan(2\pi fRC_C), \quad \text{(III-5)}$$

respectively. Here f is the frequency of the applied electric field. This problem becomes more serious as the fRC_C term becomes larger. The capacitance C_C changes depending on the concentration and the dielectric constant of the sample. In the study of liquid 1,2-dibromoethane (Chapter IV), because the dielectric constant of the sample is not great (ε_r = 2.18 [27]), the resistance R rather than the capacitance C_C is considered to be the main cause of this problem.

The thickness of the sample (i.e. the cell gap) and the applied voltage are essential for calculating the external electric-field strength. From an interference fringe pattern of the empty cell, we can estimate the actual cell gap. The positions of two adjacent peaks of the fringe pattern at wavenumber $\tilde{\omega}_1$ and $\tilde{\omega}_2$ in cm^{-1} are related to the cell gap ℓ in μm as follows:

$$2n_{\omega 1}\ell = \frac{2m-1}{2} \cdot \frac{10^4}{\tilde{\omega}_1} \quad \text{(III-6)}$$

$$2n_{\omega 2}\ell = \frac{2m+1}{2}\cdot\frac{10^4}{\tilde{\omega}_2} \qquad \text{(III-7)}$$

where $n_{\omega 1}$ and $n_{\omega 2}$ are refractive indices at $\tilde{\omega}_1$ and $\tilde{\omega}_2$ and m is an integer. Setting $n_{\omega 1} = n_{\omega 2}$ in Eqs. III -6 and III-7 yields

$$\ell = \frac{1}{2}\cdot\frac{10^4}{\tilde{\omega}_2 - \tilde{\omega}_1} \qquad \text{(III-8)}$$

The magnitude of the external electric field E_{ext} can be estimated using the cell gap so obtained and the applied voltage $V_{AA'}$. However E_{ext} is not the electric field that acts on molecules in the sample; additionally we need to consider the reaction field [1]. As a result, the internal electric filed F has the form

$$F = f' \cdot f'' E_{ext}, \qquad \text{(III-9)}$$

with

$$f' = \frac{1}{\sqrt{1+(\omega R C_c)^2}}\left(\frac{1}{\sqrt{1+(\omega R C_c)^2}} + \iota\frac{\omega R C_c}{\sqrt{1+(\omega R C_c)^2}}\right) \qquad \text{(III-10)}$$

and f'' being the local field correction. It is not an easy task to accurately estimate the factors f' and f''. According to the Onsager theory [28], for instance, the local field correction is given by

$$f'' = \frac{3\varepsilon+1}{2\varepsilon}.$$

It is known that f'' usually takes a value in between 1.1 and 1.3. The most practical way to determine the product $f' \cdot f''$ would be to use the orientational polarization signal of a polar molecule like acetone as an internal standard. Equation II-24 allows for estimation of F using the known dipole moment of the molecule provided that the molecule exists as a monomer.

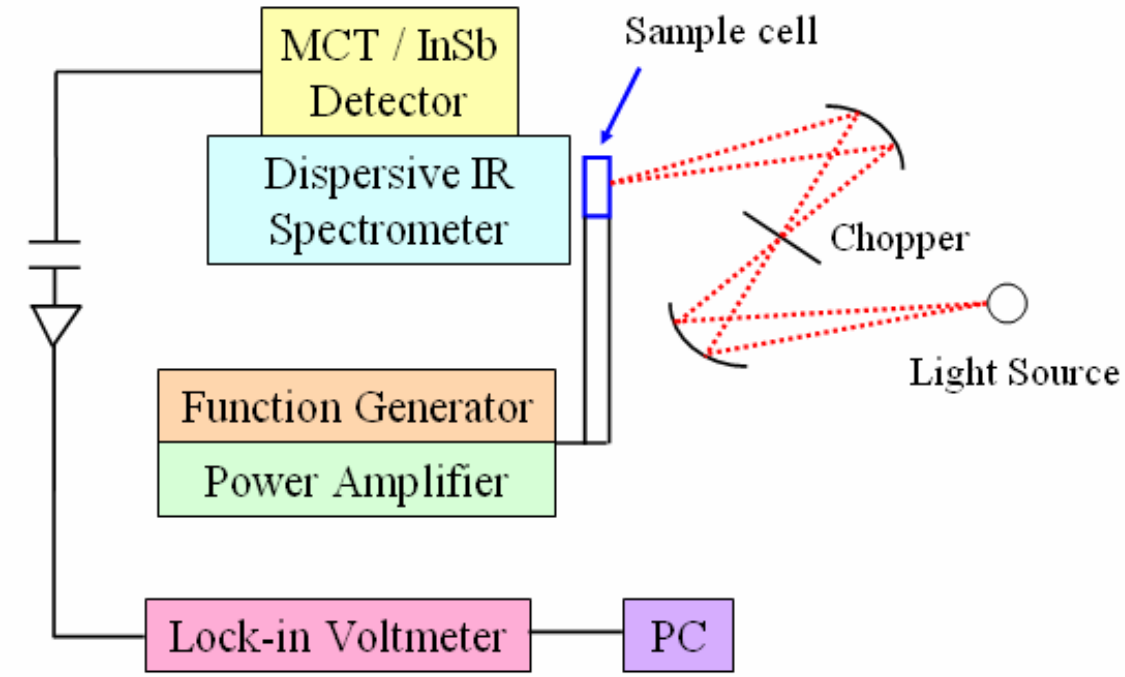

Figure III-1. Experimental setup of infrared electroabsorption spectroscopy.

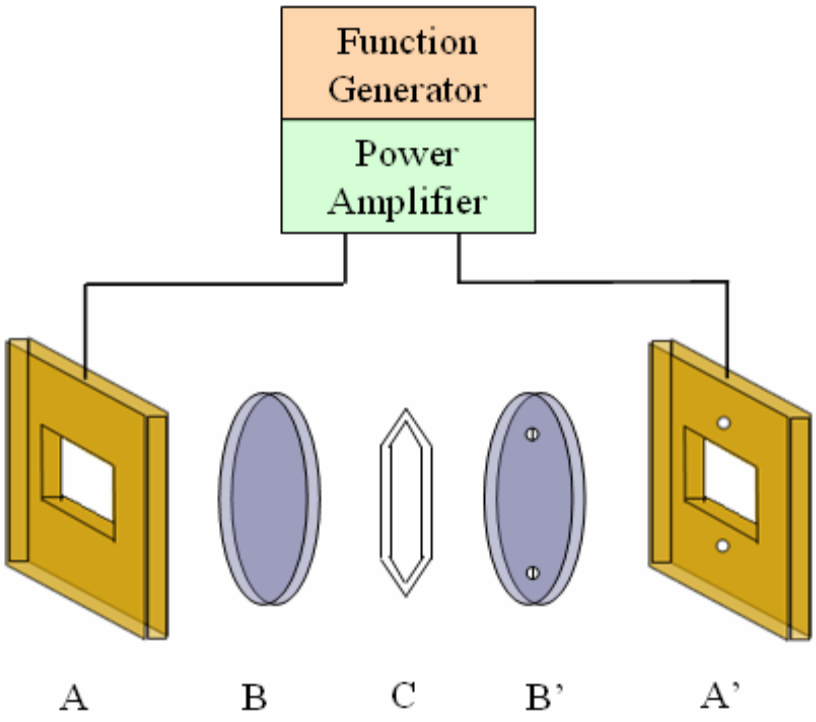

Figure III-2. Configuration of the sample cell. A/A' pair is a brass cell holder, B/B' are two silicon windows, and C is a PET film.

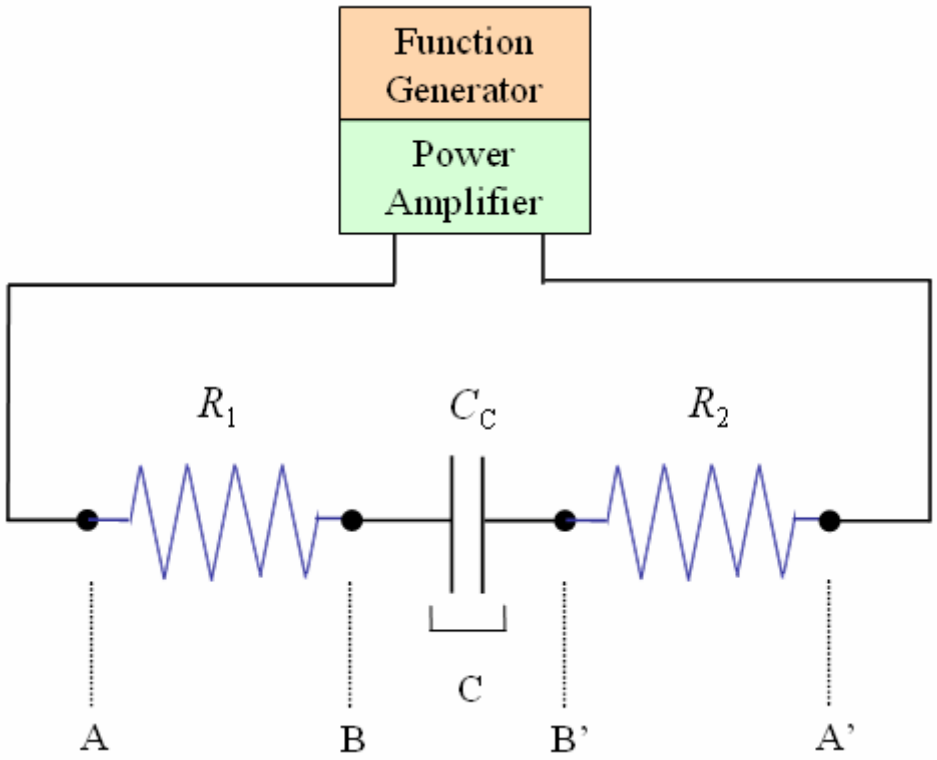

Figure III-3. RC circuit equivalent to the sample cell (Fig. III-2). R_1 is the resistance between A and B, R_2 the resistance between A' and B', and C_c the capacitance of the capacitor C.

Chapter IV

The Trans/Gauche Conformational Equilibrium and Associated Thermodynamic Parameters of Liquid 1,2-Dibromoethane

IV-1. Introduction

Internal rotation around a single bond plays an important role in molecular structures and dynamics. This phenomenon has been extensively studied by both experimental and theoretical methods. Ethane and its derivatives are prototype molecules that show internal rotation about the C–C single bond. The energy profile for internal rotation in ethane is well described by the function $V_0(1-3\cos\Phi)$, where Φ is the dihedral angle between a certain pair of opposing C–H bonds. As one of the methyl groups rotates about the central C–C bond, the molecule switches its structure three times between an eclipsed conformation (Φ = 0°, 120°, or 240°) and the preferred staggered conformation (Φ = 60°, 180°, or 300°). The former is higher in energy by about 3 kcal mol^{-1} than the latter [29]. In 1,2-disubstituted ethane, internal rotation can be somewhat restricted, and three staggered conformations are not equivalent any more. For instance, as shown in Fig. IV-1, 1,2-dichloroethane (DCE) occurs as two different stable conformers (rotational isomers): the gauche (Φ ~ 60° or 300°) and the trans (Φ ~ 180°) conformers. This rotational isomerism was first discovered by Mizushima and co-workers in 1936 [30].

1,2-Dihaloethanes (CH_2X-CH_2X) exist one trans and two gauche conformers. As can be seen from Fig. IV-1, the trans conformer has an inversion symmetry and hence has no permanent dipole moment, while the gauche conformer is of C_{2v} symmetry and possesses a permanent dipole moment. The trans/gauche equilibrium is characterized by the free energy difference ΔG between the two conformers. However the ΔG value is not easily experimentally accessible. One can measure the temperature dependence of IR bands to determine the enthalpy difference ΔH [31]. To further obtain ΔG using the well-known thermodynamic relation $\Delta G = \Delta H - T\Delta S$, the entropy difference ΔS must be somehow evaluated. In the crudest case in previous studies, ΔS was simply neglected [32]. A seemingly better treatment relies on statistical thermodynamics [33, 34], which uses partition

functions to compute the translational, vibrational, and rotational components of ΔS.

IR electroabsorption spectroscopy is a powerful alternative to those conventional techniques for experimental determination of ΔG. Hiramatsu and Hamaguchi [3, 18] used IR electroabsorption spectroscopy to determine the ΔG value of the trans/gauche equilibrium of liquid DCE. In the present study, we extend the IR electroabsorption study of the conformational equilibrium to liquid 1,2-dibromoethane (DBE). We make a comparison of the thermodynamic parameters (ΔG and ΔS) thus obtained with the previous results [3, 18] in order to gain more insight into in the intermolecular interaction in 1,2-dihaloalkanes.

Because of the different substituents (bromine versus chlorine) attached to the C-C single bond, at least the following two effects on the conformational equilibrium are expected to emerge. First, the electrostatic repulsion effect is thought to be more significant in DBE than in DCE. The larger the atomic radius, the more overlap of the two halogen atoms. Therefore, the electrostatic repulsion increases in the DBE gauche conformer, making it less stable than in the DCE gauche conformer. The other effect is on the value of the permanent dipole moment of the gauche conformer. The permanent dipole moment of the DBE gauche conformer (2.2 D in the gas phase) is indeed smaller than that of the DCE gauche (2.55 D again in the gas phase) [31], which accords qualitatively with the trend in electronegativity. The smaller dipole moment of DBE may result in a weaker electrostatic interaction with an applied electric field. These two factors mentioned above compete with each other and affect the conformational equilibrium and associated thermodynamic parameters.

IV-2. Analysis

We analyze the ΔA spectrum of liquid DBE based on the theory described in Chapter II, where three origins of the ΔA spectrum are considered. In the present case, the equilibrium change signal is of the most importance among the three.

Since an applied electric field interacts in a distinct manner with the nonpolar trans

conformer and the polar gauch conformers of DBE, it shifts the equilibrium between the gauche and the trans isomers, $\text{trans} \leftrightarrow \text{gauche}$. In the present case, the equilibrium constant K^0 is anticipated to increase as the electric field is applied, giving rise to the shift of equilibrium toward the gauche form. The equilibrium constant K^0 is related to the Gibbs free energy difference (ΔG) between the two conformers (i.e., $\Delta G = G_g - G_t$) as

$$K^0 = \frac{N_g^0}{N_t^0} = \exp\left(-\frac{\Delta G}{RT}\right), \tag{IV-1}$$

where N_g^0 and N_t^0 denote the numbers of the gauche and trans conformers, respectively, R the gas constant, and T temperature. Note that the superscript 0 always represents the physical quantity in the absence of the electric field.

When the external electric field is turned on, an additional energy $\delta\Delta G$ is introduced to ΔG via the dipolar interaction between the permanent dipole moment $\boldsymbol{\mu}_g$, of an isolated gauche conformer and the local electric field $\boldsymbol{F}$. $\delta\Delta G$ is given by $N_A \cdot \mu_g F \cos\theta$, where N_A is Avogadro's constant and θ is the angle between $\boldsymbol{\mu}_g$ and $\boldsymbol{F}$. The equilibrium constant in the presence of the applied electric field, $K^F(\theta)$, is written as

$$\begin{aligned} K^F(\theta) &= \frac{N_g^F(\theta)}{N_t^F(\theta)} = \exp\left(-\frac{\Delta G + \delta\Delta G}{RT}\right) \\ &= \exp\left[-\frac{\Delta G + N_A(\mu_g F\cos\theta)}{RT}\right] \\ &= K^0 \exp(\gamma_{equ}\cos\theta) \end{aligned} \tag{IV-2}$$

where $N_{g/t}^F(\theta)$ denotes the number of the gauche/trans conformers that are oriented along the direction θ, and $N_A k_B = R$ is used. Here, $\gamma_{equ} \equiv \mu_g E / k_B T$ is a parameter representing the electrostatic interaction for an isolated gauche molecule, responsible for the gauche/trans equilibrium change.

The total number of the gauche conformers, N_g^F, in the presence of the electric field is given by

$$N_g^F = \int_0^\pi \left\{ N_t^F(\theta) + N_g^F(\theta) \right\} \frac{N_g^F(\theta)}{N_t^F(\theta) + N_g^F(\theta)} \sin\theta \, d\theta \qquad \text{(IV-3)}$$

$N_t^F(\theta)$ is independent of θ and is equal to $\frac{1}{2} N_t^F$. Taking this into account, Eq. IV-3 yields

$$N_g^F = \int_0^\pi \left\{ \frac{1}{2} N_t^F + f(\theta, \gamma_{ori}) N_g^F \right\} \frac{K^F(\theta)}{1 + K^F(\theta)} \sin\theta \, d\theta \qquad \text{(IV-4)}$$

with $f(\theta, \gamma_{ori})$ being an anisotropy function of the form

$$f(\theta, \gamma_{ori}) = \frac{\gamma_{ori}}{\exp(\gamma_{ori}) - \exp(-\gamma_{ori})} \exp(\gamma_{ori} \cos\theta) \qquad \text{(IV-5)}$$

Here γ_{ori} is another electrostatic interaction parameter related to rotational orientation. From Eq. IV-4 and the relation $N_g^0 + N_t^0 = N_g^F + N_t^F$, we can calculate the ratios N_g^0 / N_t^0 and N_g^F / N_t^F. The absorbance change ratios for the gauche and trans conformers are then computed by $(\Delta A / A)_{g/t} = (N_{g/t}^F - N_{g/t}^0) / N_{g/t}^0 = N_{g/t}^F / N_{g/t}^0 - 1$. They have the forms [3, 18]

$$\left(\frac{\Delta A}{A} \right)_g = \frac{1}{(1 + K^0)^2} \frac{\gamma_{equ}^2}{6} + \frac{K^0}{1 + K^0} \frac{(\gamma_{equ} + \gamma_{ori})^2}{6} \qquad \text{(IV-6)}$$

and

$$\left(\frac{\Delta A}{A} \right)_t = -K^0 \left[\frac{1}{(1 + K^0)^2} \frac{\gamma_{equ}^2}{6} + \frac{K^0}{1 + K^0} \frac{(\gamma_{equ} + \gamma_{ori})^2}{6} \right] \qquad \text{(IV-7)}$$

It should be noted that the equilibrium constant K^0 can be determined by taking the ratio of $(\Delta A / A)_t$ to $(\Delta A / A)_g$. To put it in another way, it is the ratio of $\Delta A / A$ between the gauche and trans conformers that counts for determination of the thermodynamic parameters. They are accessible irrespective of the electrostatic parameters γ_{equ} and γ_{ori}, which may often contain uncertainties in the local field correction and the dipole moment in the liquid

phase. We also note that, according to Eqs. IV-6 and IV-7, the equilibrium change signal appears as the zeroth-derivative component of the band shape.

For the gauche conformer of DBE, the orientational polarization signal is also anticipated to be observed. This signal is described by [3]

$$\frac{\Delta A}{A} = \frac{\gamma_{\text{ori}}^2}{12}(1 - 3\cos^2\alpha) \tag{IV-8}$$

Here χ is set to be 90° in Eq. II-24, because the measurement is performed with normal incidence.

To summarize, the ΔA signals of the gauche and the trans conformers can be modeled by

$$\Delta A_{\text{g}} = \underbrace{\left[\frac{1}{(1+K^0)^2}\frac{\gamma_{\text{equ}}^2}{6} + \frac{K^0}{1+K^0}\frac{(\gamma_{\text{equ}}+\gamma_{\text{ori}})^2}{6}\right]\cdot A}_{\text{population change}} + \underbrace{\frac{\gamma_{\text{ori}}^2}{12}(1-3\cos^2\alpha)\cdot A}_{\text{orientational polarization}} + \underbrace{F^2\left[\frac{B_\chi}{15hc}\tilde{\upsilon}\frac{\mathrm{d}}{\mathrm{d}\tilde{\upsilon}}\frac{A(\tilde{\upsilon})}{\tilde{\upsilon}} + \frac{\mathrm{C}_\chi}{30h^2c^2}\tilde{\upsilon}\frac{\mathrm{d}^2}{\mathrm{d}\tilde{\upsilon}^2}\frac{A(\tilde{\upsilon})}{\tilde{\upsilon}}\right]}_{\text{electronic polarization}} \tag{IV-9}$$

and

$$\Delta A_{\text{t}} = \underbrace{-K^0\left[\frac{1}{(1+K^0)^2}\frac{\gamma_{\text{equ}}^2}{6} + \frac{K^0}{1+K^0}\frac{(\gamma_{\text{equ}}+\gamma_{\text{ori}})^2}{6}\right]\cdot A}_{\text{population change}} + \underbrace{F^2\left[\frac{B_\chi}{15hc}\tilde{\upsilon}\frac{\mathrm{d}}{\mathrm{d}\tilde{\upsilon}}\frac{A(\tilde{\upsilon})}{\tilde{\upsilon}} + \frac{\mathrm{C}_\chi}{30h^2c^2}\tilde{\upsilon}\frac{\mathrm{d}^2}{\mathrm{d}\tilde{\upsilon}^2}\frac{A(\tilde{\upsilon})}{\tilde{\upsilon}}\right]}_{\text{electronic polarization}} \tag{IV-10}$$

respectively.

IV-3. Methods and Materials

The experimental apparatus and the sample cell used in this study have already been described in Chapter III. Here we used a photoconductive MCT detector. A sinusoidal electric field (f = 25 kHz; $E_{0\text{-p}}$ = 1.5 × 10^7 V m^{-1}) was applied across the cell gap 5.2 μm, which was obtained from the interference fringe pattern (see Chapter III). The experiment was carried

out at room temperature. Reagent-grade 1,2-dibromoethane (DBE) was commercially obtained from Fluka (purity > 98%). Six runs were averaged to get decent ΔA spectra, which required about 2 hours.

IV-4. Results

Figure IV-2 shows the IR absorption and electroabsorption (ΔA) spectra of liquid DBE in the 1350-1140 cm^{-1} region. The three IR bands are observed in Fig. IV-2(b). They are assigned to the CH_2 wagging modes (see Table IV-1) [35]. A vector representation of the atomic displacements in the two CH_2 wagging modes of the DBE gauche conformer is shown in Fig. IV-3. In the gauche *a* normal mode, the two CH_2 groups wag out of phase, while in the gauche *b* mode they wag in phase. The gauche *a* mode has the transition moment parallel to the dipole moment ($\alpha = 0°$), and the gauche *b* mode has the transition moment perpendicular to the dipole moment ($\alpha = 90°$). A small, positive ΔA signal is observed for the gauche *a* band, and the signal is much stronger for the gauche *b* band. In contrast, the trans band shows up as a large, negative peak. Similar tendency is also found in DCE [3, 18].

In order to decompose the ΔA spectrum (Fig. IV-2(a)) into the distinct contributions described in Section IV-2, we carried out a least-squares fitting analysis. First the absorption spectrum (Fig. IV-2(b)) was fit to a superposition of three Lorentzian functions:

$$A(\tilde{\nu}) = \sum_{i=1}^{3} \frac{1}{\pi} \frac{B_i \Gamma_i}{(\tilde{\nu} - \tilde{\nu}_{0i})^2 + \Gamma_i^2} \qquad \text{(IV-11)}$$

where B_i is the area, $\tilde{\nu}_{0i}$ the peak position, and Γ_i the half width at half-maximum, of the *i*th band (*i* = 1, 2, and 3). The result of the band decomposition is displayed in Fig. IV-4, and the peak frequencies of the three bands thus obtained are listed in Table IV-1. Those frequencies accord well with those in literature [35]. Subsequently the ΔA spectrum was fit using the model functions (Eqs. IV-9 and IV-10), which consist of the zeroth, first, and second derivatives of the Lorentzian line shapes. Figure IV-4(a) shows the best fit. Here the

band parameters B_i, $\tilde{\nu}_{0i}$ and Γ_i for each band were fixed. Two adjustable parameters were used for generating the first and second derivative components of each band, and two global adjustable parameters (K^0 and $\gamma \equiv \gamma_{equ} = \gamma_{ori}$) for the zeroth derivative component of each band. In contrast with the DCE case [3, 17], assuming independent parameters of γ_{equ} and γ_{ori} does not improve much the quality of the fit, and in the spirit of trying to minimize the number of adjustable parameters in the fitting analysis, we used a single γ value as representing the electrostatic interaction parameter. K_0 and γ are determined to be 0.33 (±0.04) and 0.018, respectively. Figure IV-5 shows the contributions to the observed ΔA spectrum from the zeroth, first, and second derivative components. The zeroth-derivative spectrum is further divided into the two contributions of the equilibrium change and orientational polarization. Small but meaningful first and second derivative components indicate that the electronic polarization does contribute to some extent to the IR electroabsorption of liquid DBE.

IV-5. Discussion

The trans/gauche equilibrium change of liquid DBE is characterized by the two parameters: the electrostatic interaction parameter $\gamma = 0.018$ and the equilibrium constant $K^0 = 0.33$. γ is found to be much smaller than unity, as required (see Chapter II). The permanent dipole moment of DBE in the gas phase, $\mu_g = 2.2$ D [31], and the magnitude of the applied electric field $F = 1.3 \times 10^7$ V m^{-1} yield $\gamma = 0.02$. Taking into account the fact that we used the dipole moment in the gas phase and ignored the local field correction, the value $\gamma = 0.018$ obtained experimentally is in reasonable agreement with the theoretical estimate.

The smaller-than-unity value of K^0 evidences that DBE molecules occur in favor of the trans conformer (~75% of the molecules). This sharply contrasts with what was observed for liquid DCE: $K^0 = 1.4$, hence the gauche conformer is more favored [3]. From Eq. IV-1, the free energy difference ΔG is calculated to be 4.5 (±0.3) kJ mol^{-1}. To the best of our knowledge, this is the first ΔG value for liquid DBE determined directly by experimental

methods. There are several reports [31, 32, 34, 36] on experimental determination of the enthalpy difference ΔH. The reported ΔH values range from 2.7 kJ mol^{-1} [31] to 5.4 kJ mol^{-1} [32]. Here we use the mean value of those values and obtain ΔH = 3.7 (±1.1) kJ mol^{-1}average. The uncertainty refers to a statistical error. The large ΔH value compared with that of DCE (ΔH ~ 0.0 kJ mol^{-1} [34, 37]) accounts for the ΔG value, but despite large uncertainty in the ΔH value, the discrepancy between ΔG and ΔH still appears meaningful. Using the thermodynamic equation $\Delta G = \Delta H - T\Delta S$ with ΔH = 3.7 (±1.1) kJ mol^{-1}, we obtain the entropy difference ΔS = −2.7 J K^{-1} mol^{-1}, which is close to the value for DCE (−3.0 J K^{-1} mol^{-1} [3]). These thermodynamic parameters associated with the conformational equilibrium of liquid DBE are summarized in Table IV-2, together with those for DCE [3]. The entropy difference ΔS is the sum of the translational entropy difference ΔS_{trans}, the rotational entropy difference ΔS_{rot}, and the vibrational entropy difference ΔS_{vib}:

$$\Delta S = \Delta S_{trans} + \Delta S_{rot} + \Delta S_{vib} \qquad \text{(IV-10)}$$

Subtraction from Eq. (IV-10) of ΔS_{rot} = 1.34 J K^{-1} mol^{-1} and ΔS_{vib} = −2.78 J K^{-1} mol^{-1} [32] computed from the moments of inertia and fundamental vibrational frequencies leaves ΔS_{trans} = −1.3 J K^{-1} mol^{-1}. Instead, if we use ΔS_{rot} = 0.0 J K^{-1} mol^{-1} under the assumption that in the liquid state the rotational motion is frozen, we get ΔS_{trans} ~ 0 J K^{-1} mol^{-1}.

According to statistical thermodynamics, the translational entropy difference between the gauche and trans conformers is related to the free volumes V_g and V_t, of those conformers as follows:

$$\Delta S_{trans} = R \ln \frac{V_g}{V_t} = R \ln \frac{1 + (\Delta V / V)}{1 - (\Delta V / V)} \qquad \text{(IV-11)}$$

with the volume change from the trans to gauche conformer and the total volume being $\Delta V = V_g - V_t$ and $V = V_g + V_t$, respectively. ΔV can be determined experimentally by such methods as the pressure dependence of IR band intensities [38] and ultrasonic relaxation [32]. Also,

theoreticians can compute ΔV and use the result as a test of their theories [39]. In this study, we are able to estimate the $\Delta V/V$ values in the two limiting cases, that is, $\Delta V/V = -0.08$ for free rotation limit and $\Delta V/V \sim 0$ for frozen rotation limit. The actual volume change ratio is likely to lie in between these two limiting values. This result accords quantitatively with the $\Delta V/V$ value derived from an ultrasonic relaxation study on liquid DBE [32]. In the previous work on DCE [3], the free volume of the gauche conformer is estimated to be in between 73% (free rotation limit) and 84% (frozen rotation limit) of that of the trans conformer, which correspond to the $\Delta V/V$ values of −0.16 and −0.09, respectively. In either case, the $\Delta V/V$ value for DBE is likely to be smaller than that for DCE, which seems consistent with the prediction based on the dipolar interaction unique to the gauche conformer.

Table IV-1

Assignments, wavenumbers, conformations, and symmetries of the observed IR absorption bands of liquid 1,2-dibromoethane

Assignment[a]	Wavenumber (cm^{-1})	Conformation	Symmetry
CH_2 wag	1279	Gauche	*a*
CH_2 wag	1247	Gauche	*b*
CH_2 wag	1188	Trans	b_u

[a] Taken from [35].

Table IV-2

Thermodynamic parameters associated with the trans/gauche conformational equilibria of liquids 1,2-dichloroethane (DCE) and 1,2-dibromoethane (DBE)

	DCE		DBE[d]
	Experimental[a]	Theoretical[b]	
K^0	1.4 (±0.2)	2.06	0.33 (±0.04)
ΔG (kJ mol^{-1})	0.9 (±0.4)	−0.07	4.5 (±0.3)
ΔS (J K^{-1} mol^{-1})	−3.0		−2.7
ΔH (kJ mol^{-1})	~0.0[c]		3.7 [d] (±1.1)

[a] Taken from [3] at 293 K.

[b] Taken from [39]

[c] Taken from [34, 37].

[d] This work at 298 K.

[e] Average of the values reported in [31, 32, 34, 36, 40].

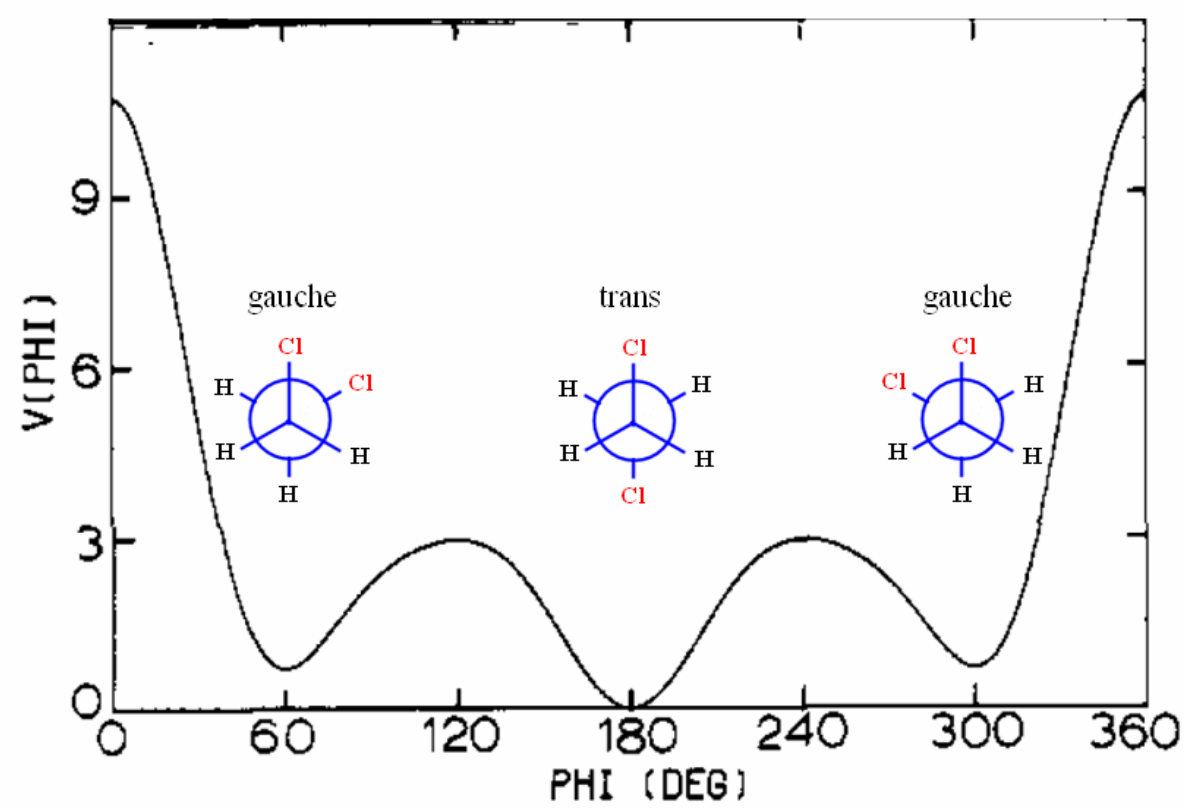

Figure IV-1. Schematic diagram of the potential energy of 1,2-dichloroethane as a function of the angle Φ (see text). Adapted from Ref [41].

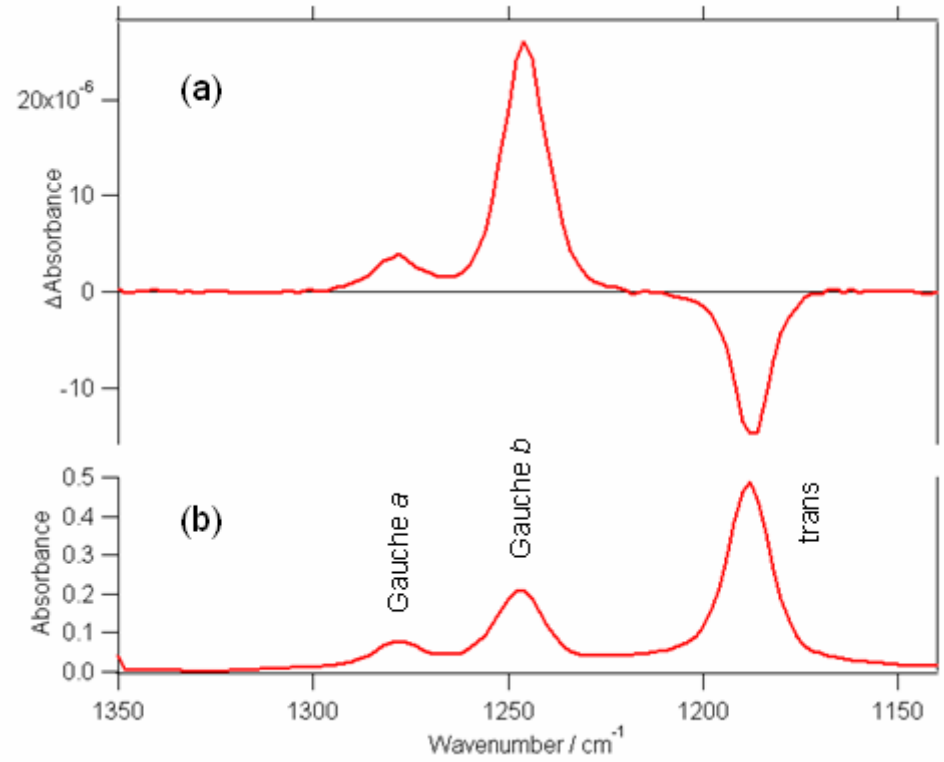

Figure IV-2. Infrared elctroabsorption (a) and absorption (b) spectra of liquid 1,2-dibromoethane. Background due to the Si reflection is subtracted in part b, and baseline is corrected in part a.

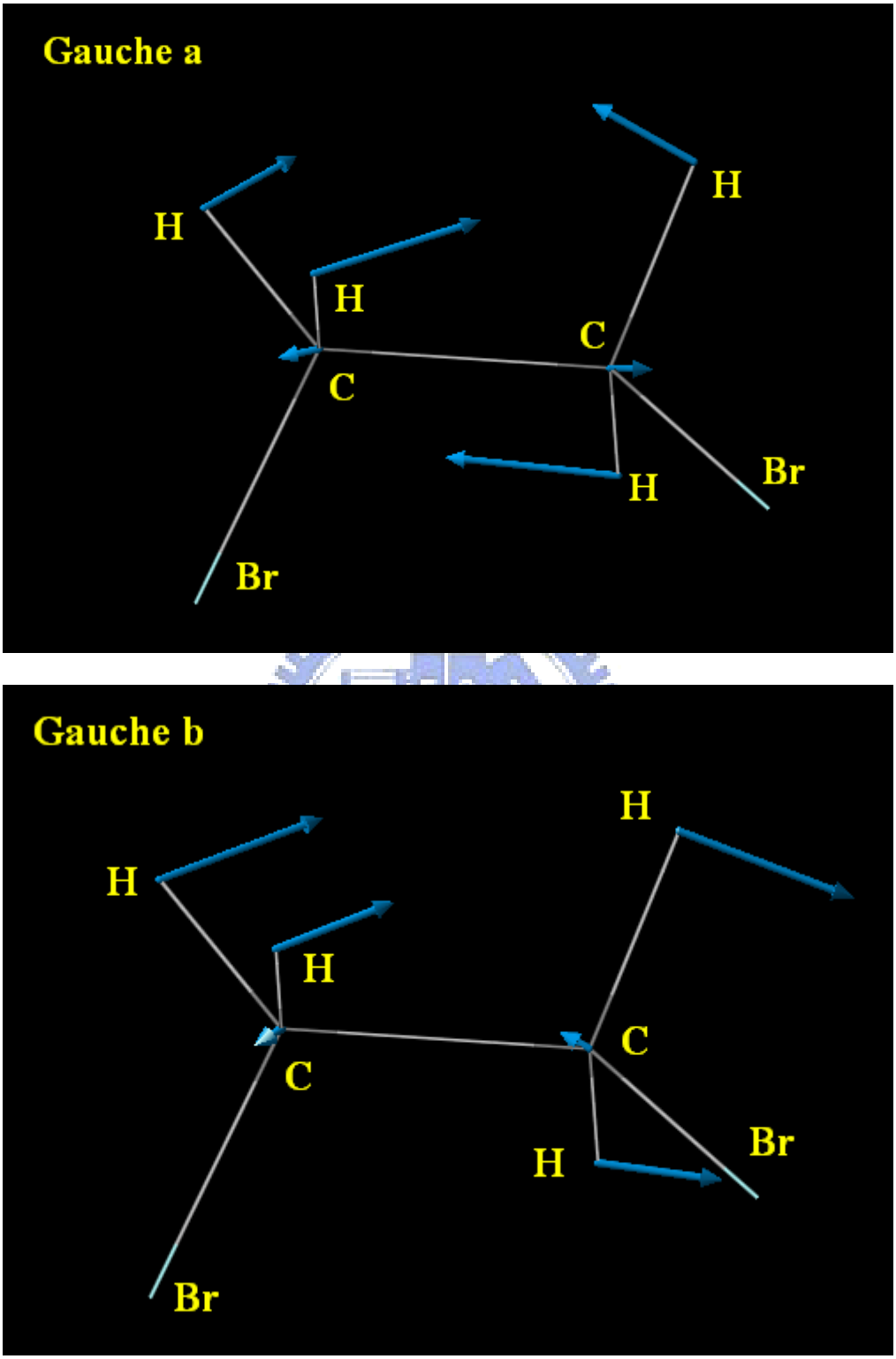

Figure IV-3. Vector representation of the atomic displacements in the CH_2 wagging modes (*a* and *b* symmetries) of the DBE gauche conformer. It was obtained from the # b3lyp/6-31g(d) level *ab initio* calculations.

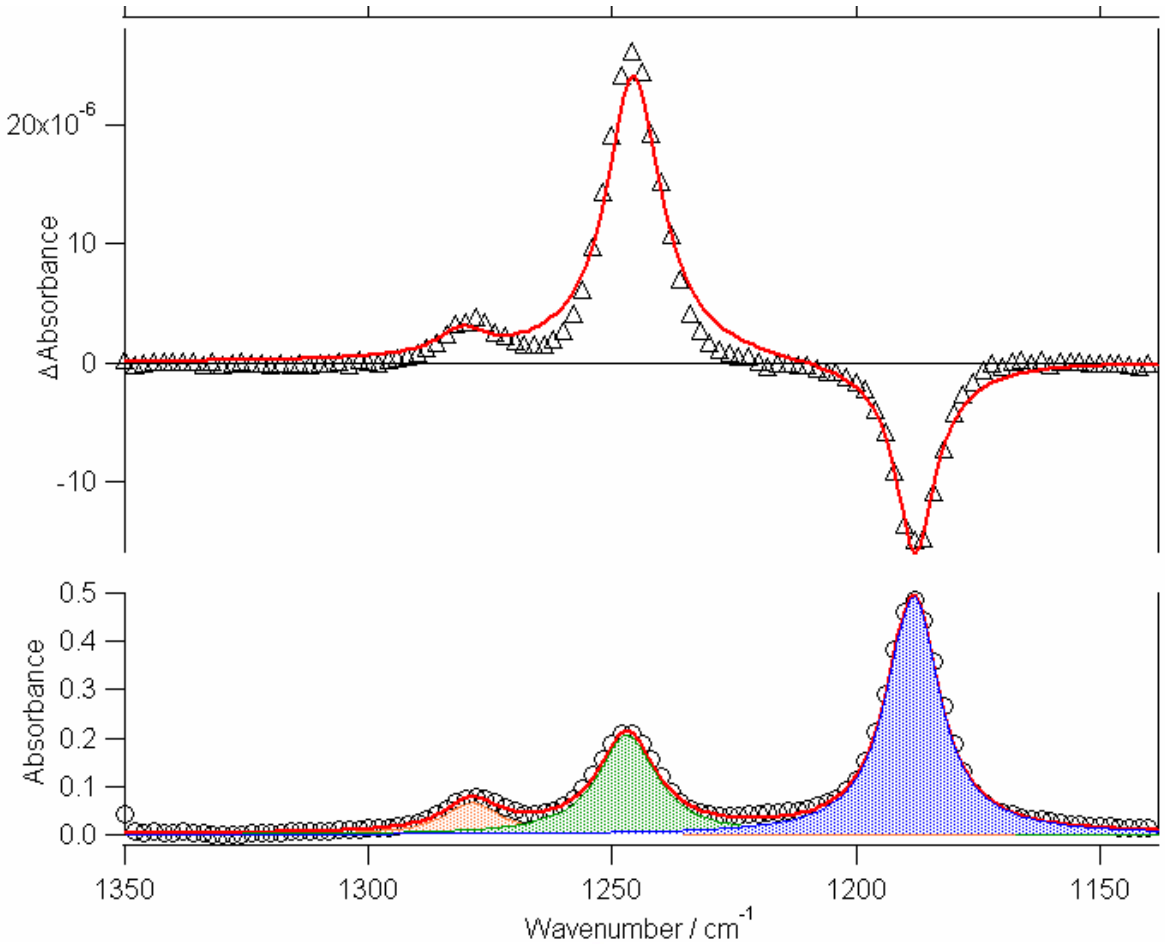

Figure IV-4. (a) Observed ΔA spectrum (Δ) of liquid 1,2-dibromoethane and the best fit (solid curve) to the model functions outlined in Section IV-2. (b) Observed absorption spectrum ($\circ$) and the best fit (solid curve) to a superposition of three Lorentzian line shapes (see text).

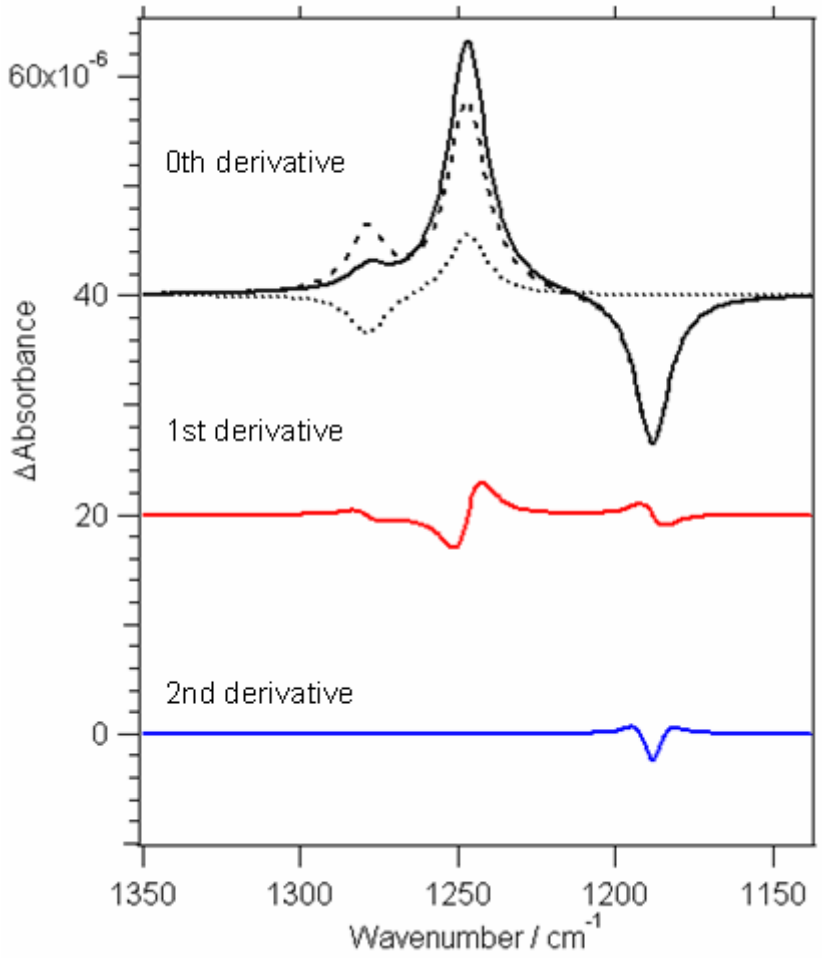

Figure IV-5. Decomposition of the Δ*A* spectrum of liquid 1,2-dibromoethane into the zeroth (solid black line), first (red line), and second (blue line) derivative components. The dashed curve shows the contribution of the equilibrium change, and the dotted curve that of the orientational polarization. For the trans conformer, the dashed curve overlaps with the solid black line.

Chapter V

The Electric Field Effect on the OH Stretching Band of Water in Reverse Micelles

V-1. Introduction

Water—the most abundant liquid in nature—plays essential roles in virtually all scientific disciplines. Water's dynamics and local environments in the liquid state are exceedingly complicated due to the three-dimensional network of hydrogen bonding. A great deal of effort has been devoted to understanding the properties of this familiar but still mysterious liquid.

From the point of view of vibrational spectroscopy, the most striking characteristic of liquid water is undoubtedly the very broad O–H stretching (ν_{OH}) band (~3100–3600 cm^{-1}). Despite much work, there still remains a central question to be convincingly answered regarding whether the ν_{OH} band is a continuous distribution of hydrogen-bonded configurations or consists of distinct subensembles. Owing to the featureless band profile, few clues can be obtained from the ν_{OH} absorption spectrum only. So some perturbation is needed to resolve different hydrogen-bonded configurations within the broad ν_{OH} band. The perturbation commonly used so far is $\nu_{OH} = 0 \rightarrow 1$ excitation (pump–probe spectroscopy; see, e.g., [42-44]). Alternatively the polar nature of water may lead us to think of applying an external electric field as a promising way. In this sense, IR electroabsorption spectroscopy is ideally suited to study the electric field effect on the ν_{OH} band and hence hydrogen-bonded configurations of water.

A technical issue that arises in water measurements results from the large IR absorption coefficient α in the ν_{OH} region [45]. The (1/e) absorption depth α^{-1} is less than 1 μm at the absorption maximum, requiring an inconveniently thin sample cell [46]. In this work, we use reverse micelle microemulsions to overcome this difficulty. As illustrated in Fig. V-1, reverse micelles encapsulate nanoscale pools of water. Sodium bis(2-ethylhexyl) sulfosuccinate (aerosol OT or AOT) is known to form spherical reverse micelles. The size of the reverse micelles is tunable by varying the molar ratio

$$W_0 = \frac{[H_2O]}{[AOT]} \quad \text{(V-1)}$$

Since reverse micelles are dispersed in a nonpolar solvent such as isooctane, CCl_4, or *n*-heptane, the ν_{OH} absorption intensity will be suppressed to a great extent. This will also alleviate another technical issue [3] related to the large dielectric constant of liquid water (ε_r = 78.3 at 298 K) compared to other liquids (e.g., ε_r of benzene and acetone are 2.3 and 20.7, respectively). Numerous experimental techniques [47-50], such as H^1NMR, time-resolved spectroscopy and infrared absorption spectroscopy, as well as molecular simulations [51-53] have been used to study unique properties of water confined in reverse micelles. Reverse micelles are also relevant to biological membranes and protein surfaces.

In this chapter, we present IR electroabsorption study of the ν_{OH} band of water in AOT reverse micelles. The ν_{OH} ΔA spectrum is well reproduced by using the zeroth derivative shapes of three Gaussian subbands within the ν_{OH} band, which may be ascribed to the field-induced change in populations of those subbands. The fact that the fractions of the higher-frequency subbands increase while that of the lower-frequency subband decreases stems from a different degree of electrostatic interaction of those subbands with the applied electric field. To the best of our knowledge, the electric field effect on the ν_{OH} band of water in reverse micelles has been observed for the first time.

V-2. Methods and Materials

V-2-1. Sample Preparation

The procedure for preparing the reverse micelle system (H_2O/AOT/*n*-heptane) runs as follows. A 0.3 M stock solution of AOT was prepared by dissolving AOT (purity > 96%, Alfa) into *n*-heptane (purity > 99%, GC grade, Riedel-de Haën) with an ultrasonicator. Molecular sieves (Type 3Å, 8-12 mesh, J. T. Baker) were put into this stock solution in order to remove the residual water, followed by filtration (pore size: 0.2 μm) to remove dusts or unwanted

particles in the stock solution. A precise volume of distilled water was then added to the stock solution such that W_0 = 15. There is an empirical linear relationship between W_0 and the diameter of the water pool in the reverse micelle (*vide infra*). Care had to be taken when adding water to the stock solution, because hasty addition of water often resulted in aggregation of the micelles. So we added water slowly (about 0.02 mL per min) to the stock solution with gentle stirring. All the samples were prepared so that they exhibited a transparent, isotropic phase at room temperature. In general, as W_0 increases, sample preparation becomes difficult. We chose the W_0 = 15 reverse micelle in this study, partly because its ν_{OH} band resembles that of pure water, and partly because it did not show any phase separation during measurements unlike samples with other W_0 values.

V-2-2. Dynamic Light Scattering (DLS)

To estimate the average diameter and size distribution of the reverse micelles, dynamic light scattering (Brookheaven 90 Plus model equipment, Brookheaven Instruments Corporation) was employed. The light source was the 632 nm output of a He-Ne laser, and the laser power was 35 mW. Here, the refractive index of pure *n*-heptane was used to analyze the data.

V-2-3. Spectroscopic Measurements

The experimental apparatus and the sample cell have already been described in Chapter III. Briefly, a 25 KHz sinusoidal electric field was applied across the cell gap of 5.2 μm, which was calculated from the interference fringe pattern. In this work the InSb detector was used instead of the MCT detector. For IR absorption measurements without an applied electric field, a sample cell composed of CaF_2 windows and a lead spacer (50 μm thick) were also used. All the experiments were carried out at room temperature (298 K). During the measurements, we paid special attention to keeping the sample flow through the cell, which was more difficult than in the case of 1,2-dibromoethane due to the higher viscosity of the

reverse micelle sample.

V-3. Results

V-3-1. Dynamic light scattering

Figure V-2 shows the distribution of the diameter of the W_0 = 15 reverse micelle obtained from the dynamic light scattering (DLS) measurement. The average diameter d is estimated as d = 6.4 (±1.0) nm. For AOT reverse micelles in isooctane, the linear relationship

$$d = 0.29\ W_0 + 1.1 \text{ (nm)} \qquad \text{(V-2)}$$

applies to reverse micelles in the range W_0 = 2–20 [54]. This empirical formula gives the value d = 5.4 nm for W_0 = 15, so the d = 6.4 nm observed here is considered to be a reasonable size. Moreover the size distribution of the reverse micelle looks uniform. The number of water molecules contained in the water nanopool is roughly 2500.

V-3-2. Infrared absorption and electroabsorption spectra

Figure V-3 compares the IR absorption spectra in the ν_{OH} region of a 0.3 M stock solution of AOT (i.e., W_0 = 0) and of the W_0 = 15 reverse micelle. Virtually no absorption is seen in this region of the stock solution, ensuring that residual water is effectively removed from the solution. To determine the residual water content, we need to use Karl-Fisher titration, which we did not perform.

Typical infrared absorption and electroabsorption (ΔA) spectra measured with 2.9×10^6 V m^{-1} are shown in Fig. V-4. In the absorption spectrum, the immense C–H stretching bands (around 2920 cm^{-1}) of AOT are observed together with the much weaker ν_{OH} band (around 3440 cm^{-1}) of water. In contrast, the ΔA spectrum is dominated by the ν_{OH} signal. The ΔA spectrum of the ν_{OH} band shows a characteristic bipolar feature with intensity apparently moving from the red to the blue. This bipolar feature is reminiscent of hydrogen bond weakening [44, 55]. The ΔA spectrum appears to evidence at least two different hydrogen-bonded configurations of water in the reverse micelle, showing remarkably

different ΔA signals (the positive peak at 3550 cm^{-1} and the negative peak at 3250 cm^{-1}) within the ν_{OH} band. Hereafter we concentrate on the ν_{OH} band, and the C–H stretching bands are left for future studies.

V-3-3. Electric-Field Strength Dependence

The electric-field strength dependence of the ΔA spectrum is shown in part a of Fig. V-5. As argued in Chapter II, ΔA signals observed in our experiment are proportional to the square of the electric-field strength F. Inspection of part a of Fig. V-5 shows that the overall shape of the ΔA spectrum remains nearly the same for those three field strengths and only the amplitude varies. Part b of Fig. V-5 plots the ΔA signals (the mean values calculated for the ranges 3548–3516 cm^{-1} and 3308–3276 cm^{-1}) as a function of F^2. The experimental data are well fit to a straight line.

V-4. Discussion

There has been a long-standing debate about how the large width (FWHM ~500 cm^{-1}) of the ν_{OH} band of water can be interpreted. A widespread notion has been the idea of presuming subbands (or subensembles), which arise from distinctly different hydrogen-bonded configurations [56-58]. Although this subband picture has not been fully convinced by either experiment or theory, here we analyze our data based on it. The absorption spectrum obtained with the thicker spacer is decomposed into three Gaussian subbands:

$$A(\tilde{\nu}) = \sum_{i=1}^{3} B_i \exp\left[-\left(\frac{\tilde{\nu} - \tilde{\nu}_{0i}}{\Gamma_i}\right)^2\right] \qquad \text{(V-3)}$$

where B_i is the peak height, $\tilde{\nu}_{0i}$ the peak position, and Γ_i the bandwidth of the ith band (i = 1, 2, 3). Here we used Gaussian line shapes because of the inhomogeneous broadening of the ν_{OH} transition [59] The reason for using the thicker (50 μm) spacer is that the signal-to-noise ratio of the absorption spectrum taken with the same sample cell as in the ΔA measurement is not high enough to facilitate accurate band decomposition. Note, however,

that correction for the difference in the cell gaps (50 μm vs. 5.2 μm) needs to be considered when relating that spectrum to the ΔA spectrum. The decomposition result is shown in Fig. V-6. For comparison's sake, a fit using two Gaussian subbands is plotted in Fig. V-6(b), which does not reproduce well the spectrum. Here we denote the distinct three subbands H_1, H_2, and H_3 in order of decreasing the frequency. The frequency, amplitude, and bandwidth of each component so obtained are listed in Table V-1, together with the frequencies obtained by Onori et al. [60] for reference. Except for the subband H_1, the frequencies determined in the present study are in good agreement with those reported in the literature [61]. In a reasonably well-accepted view [57, 62, 63], these bands can be assigned to the "bound water", which is made up of water molecules associated with the headgroups that form an outer shell of the water nanopool, and the "bulk (or bulk-like) water", which exist in the core of the micelle (see Fig. V-1).

The ΔA spectrum (Fig. V-4) can be represented by a linear combination of the zeroth, first, and second derivative shapes of the absorption bands for H_1–H_3. Even if we fix the line-shape parameters (amplitudes, peak positions, and widths) to the values tabulated in Table V-1, there would be 9 coefficients left. 6 out of 9 coefficients are responsible for the first and second derivative components, and our previous studies [3, 20] reveal that these components originate from the electronic polarization. So we discuss the electronic polarization signal first.

According to Eq. II-26, the pure electronic polarization contribution to the zeroth derivative component is given by

$$\frac{\Delta A}{A} = -\frac{F^2}{10 k_B T}(\alpha_{gm} - \bar{\alpha}_g) \qquad \text{(V-4)}$$

where $\chi = 90^\circ$ is used. $\Delta A / A$ is related to the difference between the component of the polarizability along the transition moment (α_{gm}) and the average value of the polarizability

($\bar{\alpha}_g \equiv \mathrm{Tr}\alpha_g / 3$). For the $\alpha = 0^o$ mode, use of the experimental values α_{xx} = 1.5284 Å^3, α_{yy} = 1.4146 Å^3, and α_{zz} = 1.4679 Å^3 [64] gives α_{gm} = 1.4146 Å^3 and $\bar{\alpha}_g$ = 1.4703 Å^3, where the molecule is set on the *xy*-plane with the permanent dipole moment being along the *y*-axis. Substitution of the values of α_{gm}, $\bar{\alpha}_g$, $F = 2.9 \times 10^6$ V m^{-1}, $k_B = 1.38 \times 10^{-23}$ J K^{-1}, and T = 298 K into Eq. V-4 yields $\Delta A / A \approx 1 \times 10^{-10}$. The resultant ΔA is five orders of magnitude smaller than the observed signal. The first- and second-derivative components of the electronic polarization signal are expected to be comparable to or even smaller than the zeroth-derivative component [3], so it follows that the electronic polarization signal can be disregarded in the present case.

Now we are able to focus on the zeroth derivative component where the contribution of the electronic polarization has already been ruled out. Let us consider the orientational polarization ΔA signal as a candidate for the zeroth derivative component. The ΔA signal is estimated from Eq. II-23. Given that the angle $\alpha = 0^o$ (corresponding to the symmetric ν_{OH} mode), T = 298 K, $F = 2.9 \times 10^6$ V m^{-1}, and $\mu_P = 1.85$ D [65], the magnitude of the absorbance change ratio $|\Delta A/A|$ is approximately 3×10^{-6}. The absorbance of the ν_{OH} band is at most 0.1 (see Fig. V-4), so that ΔA is of the order of 10^{-7}, which is much smaller than the observed signal. Thus the orientational polarization contribution can be disregarded in the present case. The same conclusion is reached if the $\alpha = 90^o$ mode (the asymmetric ν_{OH} transition) is considered. Strictly speaking, for liquid water, assignment of the symmetric or asymmetric stretching to the ν_{OH} vibration is ambiguous; the ν_{OH} band should be viewed as being inhomogeneously broadened. Nevertheless we believe that the discussion here is valid as long as the order of the signal is concerned.

The discussion given above leaves only the possibility that the observed ΔA signal originates predominantly from the equilibrium population change [20]. We assume the

equilibrium among the three ν_{OH} subbands H_1–H_3:

$$H_1 \xleftrightarrow{K_{12}} H_2 \xleftrightarrow{K_{23}} H_3 \qquad \text{(V-5)}$$

where K_{12} and K_{23} are the equilibrium constants between H_1 and H_2 and between H_2 and H_3, respectively. The ΔA spectrum shown in Fig. V-4(a) was fit by using the zeroth derivative shapes of the three Gaussian subbands plus baseline. We chose the data measured with field strength of 2.9×10^6 V m^{-1}, since it is found in Fig. V-5 that the ν_{OH} ΔA spectrum changes only its amplitude as the electric-field strength varies. The overall fit as well as the spectra corresponding to components H_1–H_3 is displayed in Fig. V-7. The figure shows that the fractions of H_1 and H_2 increase, while that of H_3 decreases. The absorbance change ratios for components H_1–H_3 are determined as $(\Delta A/A)_{H1} = 6.4 \times 10^{-5}$, $(\Delta A/A)_{H2} = 4.6 \times 10^{-5}$, and $(\Delta A/A)_{H3} = -3.3 \times 10^{-6}$, respectively. Obviously the relation

$$\left(\frac{\Delta A}{A}\right)_{H_1} + \left(\frac{\Delta A}{A}\right)_{H_2} + \left(\frac{\Delta A}{A}\right)_{H_3} = 0 \qquad \text{(V-6)}$$

is not fulfilled. Equation V-6 holds if and only if the molar extinction coefficients of subbands H_1–H_3 are all the same. The molar extinction coefficient might be affected by hydrogen-bonded configuration. As a result, the molar extinction coefficients of the subbands within the same ν_{OH} manifold could differ from each other. The signs of $\Delta A/A$ for H_1–H_3 indicate that applying an electric field may cause hydrogen bonds to break (or weaken), giving rise to apparent increase in the "bound water" and decrease in the "bulk water". The headgroups of AOT molecules are more negatively charged after interacting with the applied electric field and enhance the H-bonding of H_3. Due to the stronger H-bonding of H_3, the populations of H_3 and H_2 may increase and that of H_1 decreases. As in our previous work on *p*-nitroaniline in acetonitrile/CCl_4 [20], the control of the distribution of water molecules with distinct hydrogen-bonded configurations has been demonstrated. An improved version of the theory described in Chapter IV will enable us to gain quantitative insights into the equilibrium

constants K_{12} and K_{23} and the effective dipole moments. Studies along this line are now under way.

Table V-1

Labels, wavenumbers, amplitudes, and widths of Gaussian subbands of the ν_{OH} band of water in the $W_0 = 15$ reverse micelle.

Label	Wavenumber (cm^{-1})		Relative amplitude	Width (cm^{-1})
	This work	Previous work[a]		
H_1	3575 (±4)	3603 (±6)	0.5 (±0.1)	73 (±5)
H_2	3461 (±6)	3465 (±5)	1.2 (±0.2)	120 (±12)
H_3	3306 (±20)	3330 (±20)	1.1 (±0.1)	200 (±12)

[a] Taken from [61].

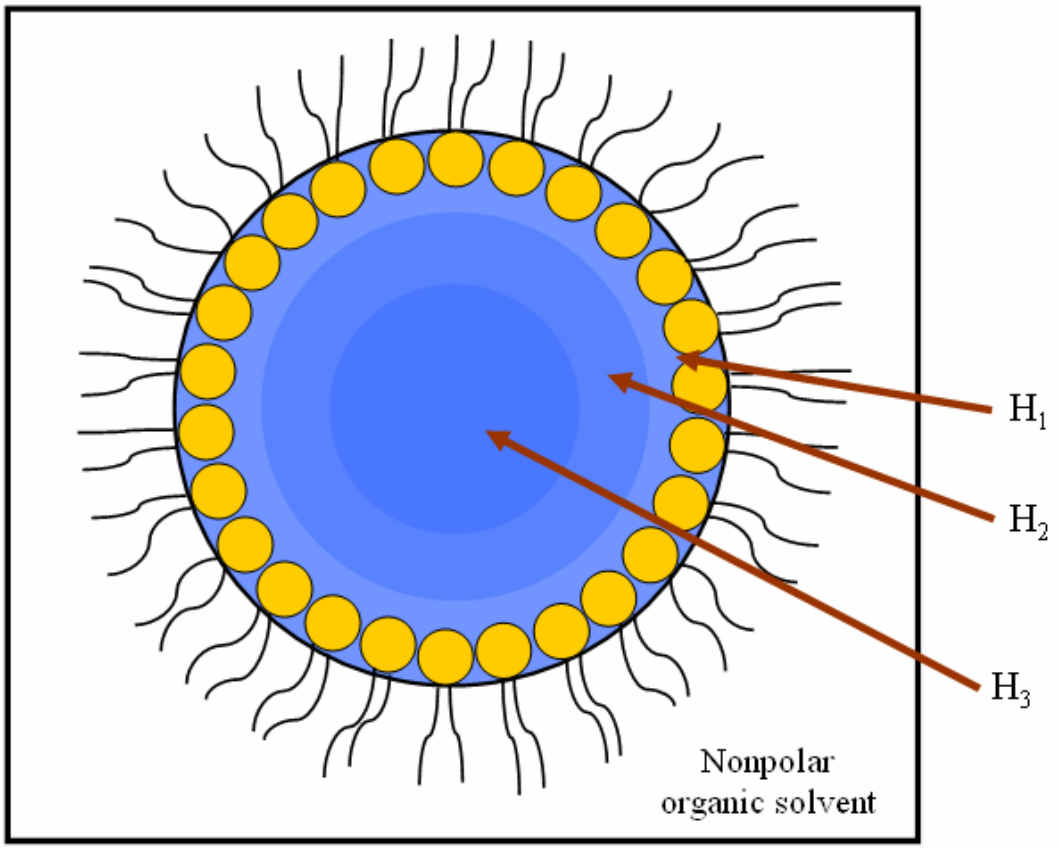

Figure V-1. Illustration of water in a reverse micelle. The hydrophilic headgroups of the surfactant molecules form a spherical nanopool that confines water molecules inside and isolates them from the bulk of a nonpolar solvent. It is suggested from previous studies that there exist three kinds of water in the nanopool: the water strongly bound to the headgroups (denoted H_1 in this thesis), the water residing an outer layer of the nanopool (H_2), and the bulk-like water near the core of the micelle (H_3).

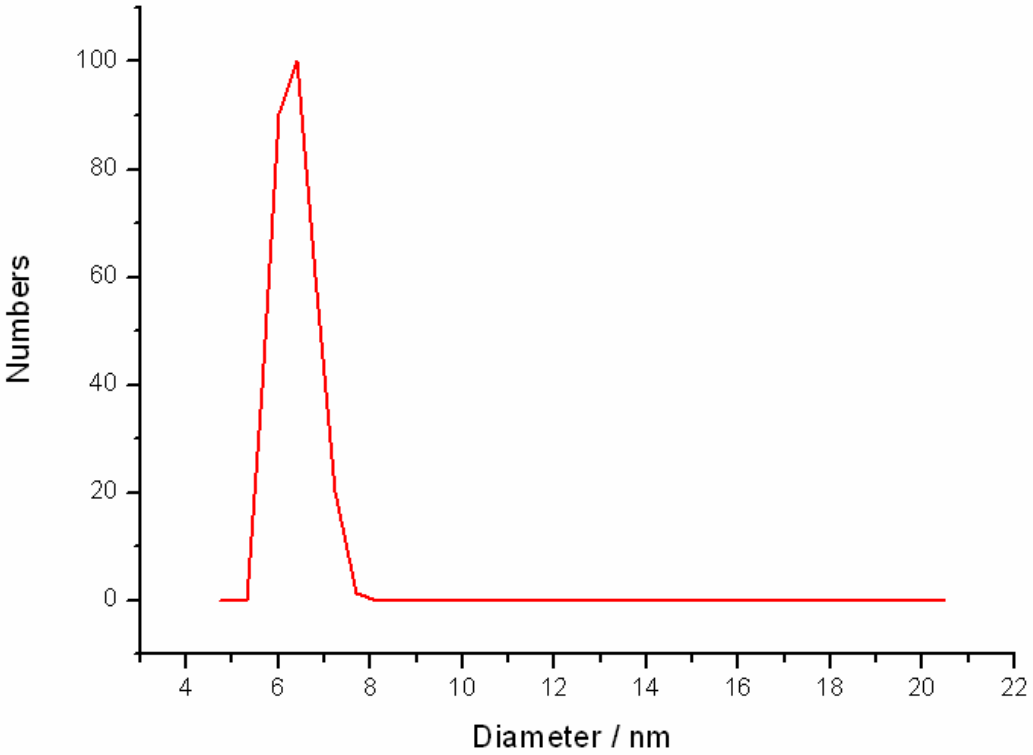

Figure V-2. Distribution pattern of the diameters of the W_0 = 15 reverse micelle.

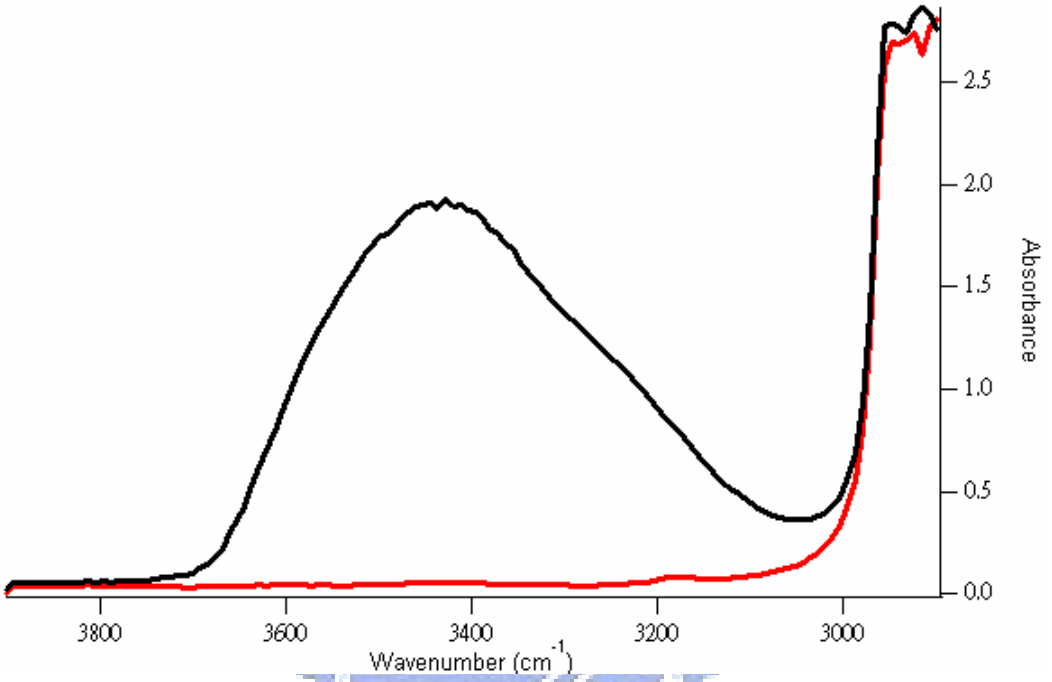

Figure V-3. Comparison of infrared absorption spectra in the ν_{OH} region of the stock solution (W_0 = 0, red curve) and the W_0 = 15 reverse micelle (black).

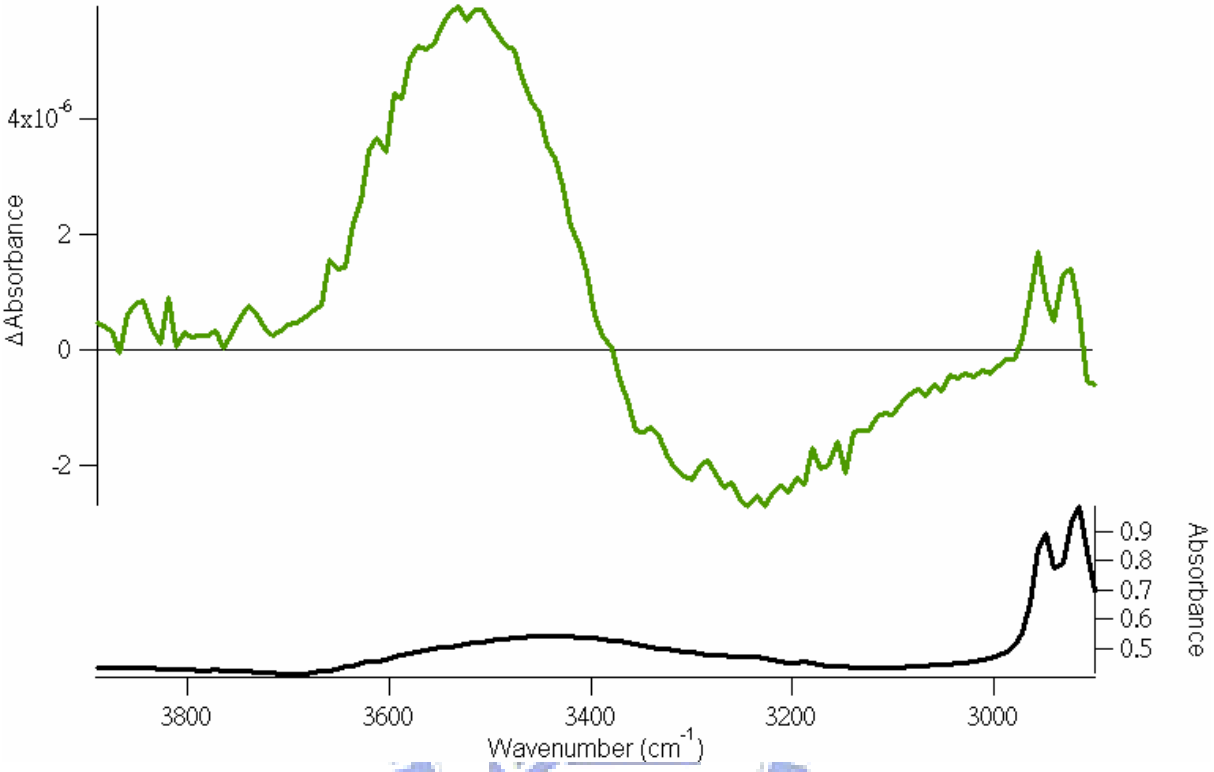

Figure V-4. Infrared absorption (black) and electroabsorption (green) spectra in the wavenumber region 3900–2900 cm^{-1} of the W_0 = 15 reverse micelle. The ΔA spectrum was measured with 2.9×10^6 V m^{-1}.

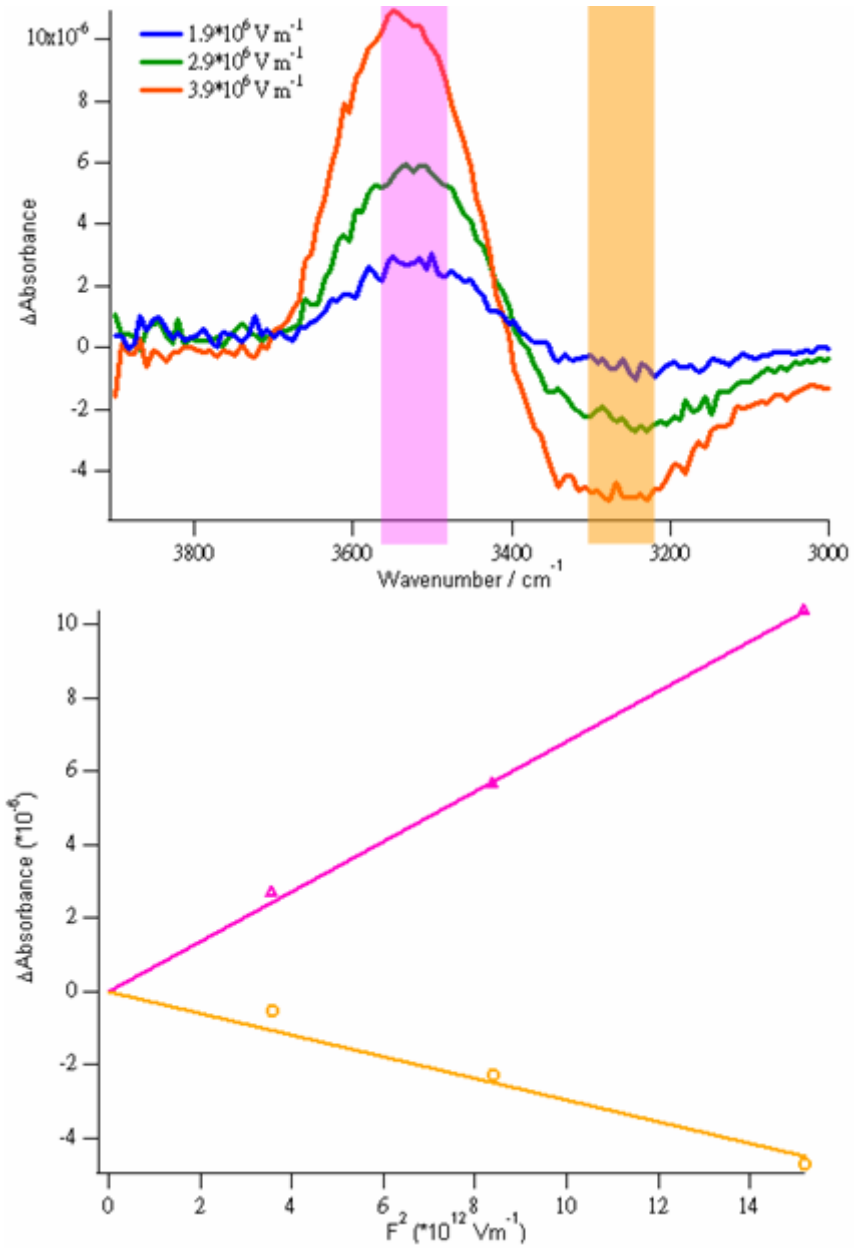

Figure V-5. (a) A series of infrared electroabsoption spectra of the ν_{OH} band of water in the $W_0 = 15$ reverse micelle, measured with electric field strengths of 1.9×10^6 V m^{-1}, 2.9×10^6 V m^{-1}, and 3.9×10^6 V m^{-1}. (b) External field strength dependence of the electroabsorption signals of the ν_{OH} band. Triangles represent the mean ΔA values in the 3548–3516 cm^{-1} range and circles represent those in the 3308–3236 cm^{-1} range. The solid lines show fits to a straight line.

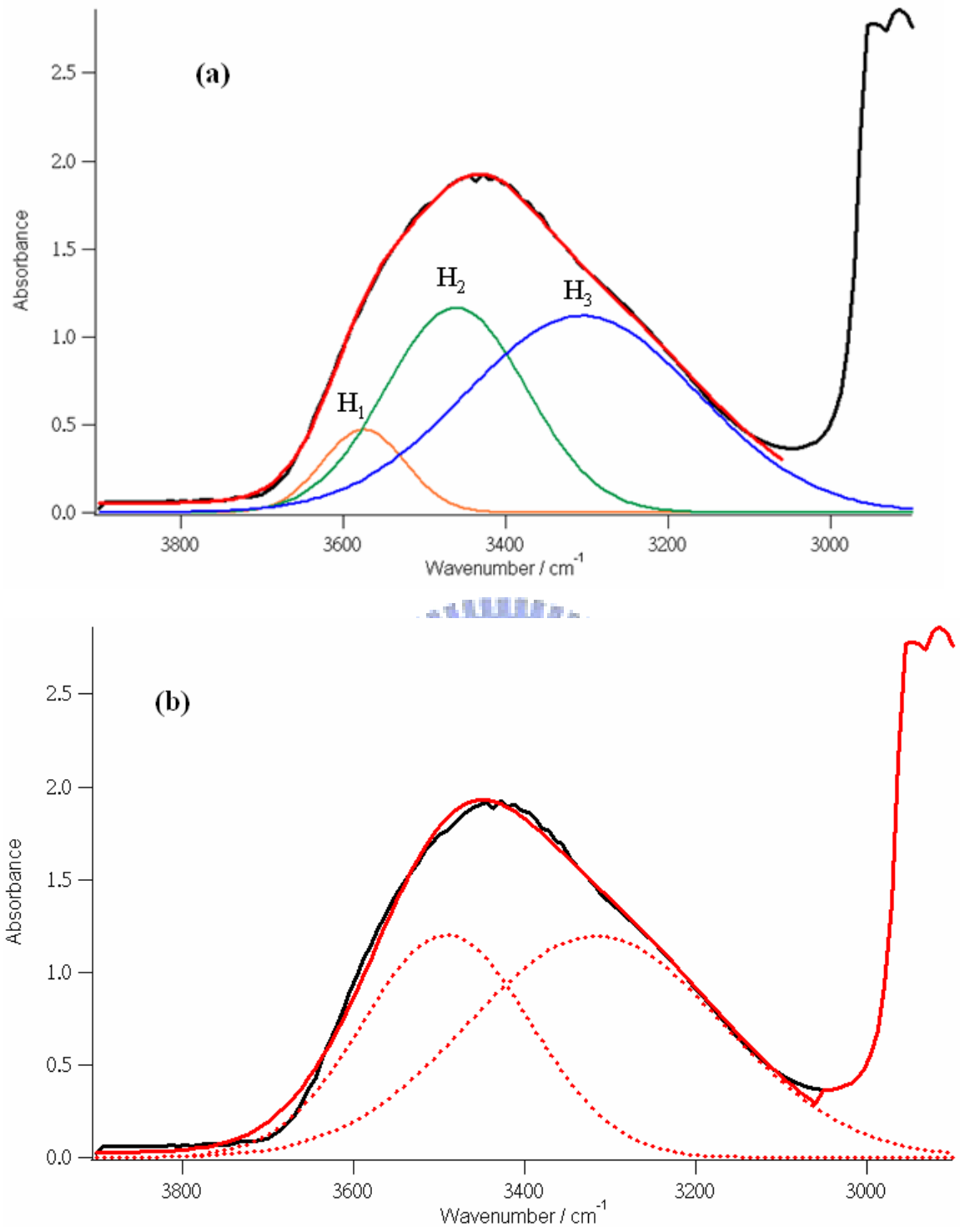

Figure V-6. (a) Decomposition of the ν_{OH} band of water in the W_0 = 15 reverse micelle into three Gaussian subbands. The ν_{OH} band of the IR absorption spectrum (black curve) measured with a spacer 50 μm thick was fit by using three Gaussian subbands termed H_1, H_2, and H_3. The best fit is shown by the red curve. (b) A two-Gaussian fit does not reproduce well the observed spectrum.

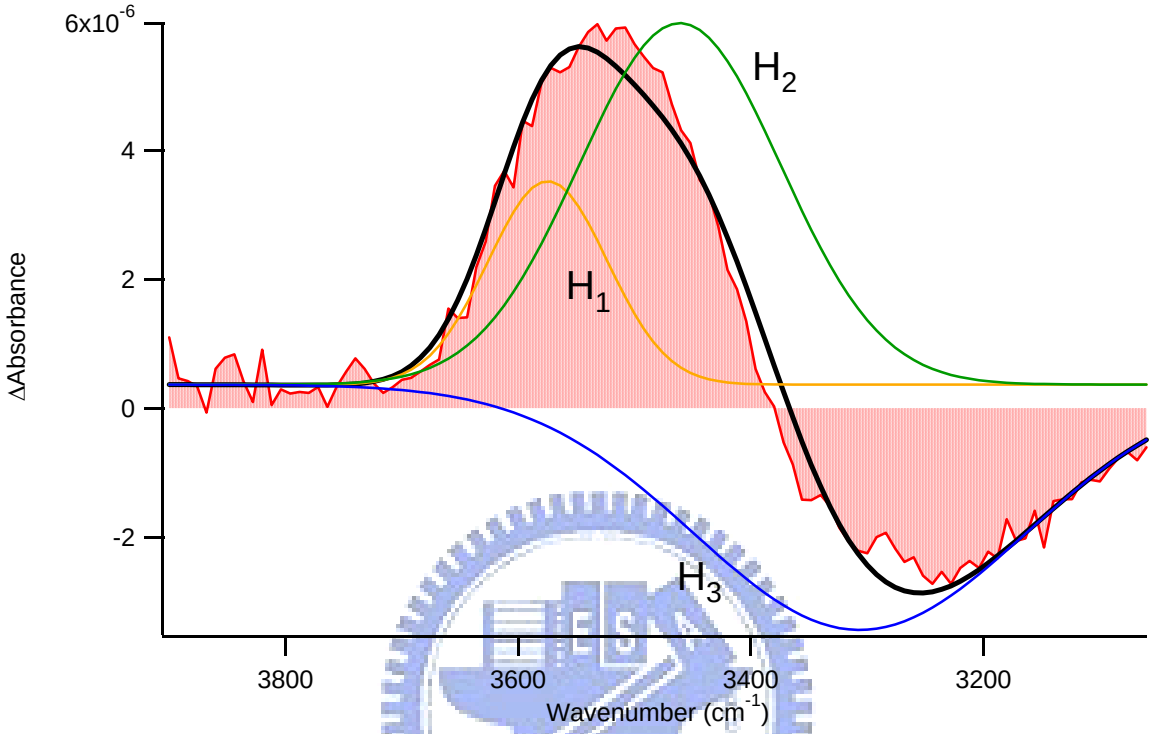

Figure V-7. Fitting analysis of the ΔA spectrum in the ν_{OH} region of water in the W_0 = 15 reverse micelle with 2.9 × 10^6 V m^{-1}, by using the zeroth derivative shapes of the Gaussian subbands H_1–H_3 determined in Fig. V-6. The black curve is the best fit.

Chapter VI

Conclusion

In this thesis, the author has presented IR electroabsorption studies of liquid 1,2-dibromoethane (DBE) and water in AOT reverse micelles. Here the major outcomes and future perspectives are briefly summarized.

In Chapter IV, the gauche/trans conformational equilibrium and associated thermodynamic parameters of liquid DBE were studied. The observed ΔA spectrum in the CH_2 wagging region was analyzed on the basis of the model descrbied in Chapter II, and we obtained the equilibrium constant $K^0 = 0.33$ (±0.04) and the electrostatic interaction parameter $\gamma = 0.018$. As opposed to liquid 1,2-dichloroethane, DBE molecules occurs in favor of the trans conformer. The Gibbs free energy difference ΔG between the two conformers was experimentally determined for the first time as 4.5 (±0.3) kJ mol^{-1}. The corresponding entropy difference ΔS, which for the condensed phase was hardly accessible by experiment, was obtained to be −2.7 J K^{-1} mol^{-1}. We used this ΔS value to estimate the ratio of the free volumes of the gauche and the trans conformers of liquid DBE: the free volume of the gauche conformer is 86 % (free rotation limit) or ~100 % (frozen rotation limit) of that of the trans conformer. Those values for liquid DBE are smaller than those for liquid DCE (73% and 84%, respectively) [3]. This finding is in qualitative agreement with the smaller dipole moment of the DBE gauche conformer compared to the DCE gauche conformer.

One can utilize the sensitivity of ΔA spectra to rotational isomerism to experimentally assign IR bands of long-chain hydrocarbons or polymers that have remained unidentified. It will be interesting to do a systematic study of IR electroabsorption spectroscopy on such hydrocarbons or polymers.

In Chapter V, we discussed the electric-field effect on the O–H stretching band of water in AOT reverse micelles. The ν_{OH} band of water in the W_0 = 15 reverse micelle was decomposed into three Gaussian subbands that correspond to distinct hydrogen bonded configurations in the nanopool of the reverse micelle. The ΔA spectrum of water in the W_0 =

15 reverse micelle was analyzed by assuming that there is an equilibrium among those three kinds of water and that the equilibrium shifts due to the applied electric field. It is found that, upon application of the electric field, the fraction of water with the highest ν_{OH} frequency increases, while those of the other two water species decrease. The validity of our assumption made in the present work can be checked through the W_0 dependence of the ΔA spectrum, which is the next step of our study.

References

1. G.U. Bublitz and S.G. Boxer, *Annu. Rev. Phys. Chem.*, 1997. **48**: p. 213.
2. N. Ohta, *Bull. Chem. Soc. Jpn.* , 2002. **75**: p. 1637.
3. H. Hiramatsu and H. Hamaguchi, *Appl . Spectrosc.*, 2004. **58**: p. 355.
4. S.G. Boxer, *J. Phys. Chem. B*, 2009. **113**: p. 2972.
5. W. Liptay, *Angew. Chem. Int. Ed. 8, 177 (1969)*.
6. W. Liptay, *in Excited States (E. C. Lim, ed.) Academic Press*, 1974.
7. Lias N. Silverman, et al., *J. Phys. Chem. A*, 2008. **112**: p. 10244.
8. Nobuhiro Ohta, et al., *J. Phys. Chem.*, 1996. **100**: p. 16466.
9. Tomokazu Yoshizawa, et al., *J. Phys. Chem. B*, 2004. **108**: p. 19132.
10. Mohan Singh Mehata, et al., *J. Phys. Chem. A*, 2006. **110**: p. 10985.
11. Mohan Singh Mehata1, et al., *J. Photochem. Photobio. A: Chemistry* 2009. **204**: p. 39.
12. Paul Handler and D.E. Aspnes, *The Journal of Chemical Physics* 1967. **47**: p. 473.
13. Chattopadyay, A. and S.G. Boxer, *J. Am. Chem. Soc.*, 1995. **117**: p. 1449.
14. Steven S. Andrews and Steven G. Boxer, *J. Phys. Chem. A*, 2000. **104**: p. 11853.
15. Eun Sun Park and Steven G. Boxer, *J. Phys. Chem. B*, 2002. **106**: p. 5800.
16. Ian T. Suydam, et al., *Science*, 2006. **313**: p. 200.
17. H. Hiramatsu, C. Kato, and H. Hamaguchi, *Chem. Phys. Lett.*, 2001. **347**: p. 403.
18. H. Hiramatsu and H. Hamaguchi, *Chem. Phys. Lett.*, 2002. **364**: p. 457.
19. Y. K. Min, H. Hiramatsu, and H. Hamaguchi, *Chem. Lett.* , 2002. **68**.
20. Shinsuke Shigeto, Hirotsugu Hiramatsu, and Hiro-o Hamaguchi, *J. Phys. Chem. A*, 2006. **110**: p. 3738.
21. I-Chun Lee, Hiro-o Hamaguchi, and S. Shigeto, *Chem. Phys. Lett.*, 2008. **466**: p. 144.
22. Morgan Ponder and Richard Mathles, *J. Phys. Chem.*, 1983. **87**: p. 5090.
23. Erko Jalviste and Nobuhiro Ohta, *J. Photochem. Photobio. C*, 2007. **8**: p. 30.

24. A.T. Fafarman, et al., *J. Am. Chem. Soc.*, 2006. **128**: p. 13359.

25. <http://www.thinksrs.com/downloads/PDFs/ApplicationNotes/AboutLIAs.pdf>.

26. D. P. Blair and P.H. Sydenham, *J. Phys. E: Scientific Instruments*, 1975. **8**: p. 621.

27. R. K. Sreeruttun and P. Ramasami, *Physics and Chemistry of Liquids*, 2006. **44**: p. 315.

28. H. Flöhlich, *Theory of Dielectrics, 2nd ed.; Oxford at the Clarendon Press*, 1960.

29. J. D. Kemp and K. S. Pitzer, *J. Chem. Phys.*, 1936. **4**: p. 749.

30. S. Mizushima, Y. Morino, and S. Noziri, *Nature*, 1936. **137**: p. 952.

31. Y. Morino, et al., *J. Chem. Phys.*, 1950. **18**: p. 754.

32. K. Takagi, P. K. Choi, and W. Seki, *J. Chem. Phys.*, 1983. **79**: p. 964.

33. Mizushima, S., et al., *J. Chem. Phys.*, 1949. **17**: p. 591.

34. K. Tanabe, *Spectrochim. Acta*, 1972. **28A**: p. 407.

35. T. Shimanouchi, *Tables of Molecular Vibrational Frequencies Volume I, National Bureau of Standards, 1972.*

36. A. A. Stolov, N. V. Kohan, and A. B. Remizov, *Vib. Spectrosc.*, 1997. **14**: p. 35.

37. A. Wada, *J. Chem. Phys.*, 1954. **22**: p. 198.

38. Y. Taniguchi, et al., *J. Chem. Phys.*, 1981. **75**: p. 4815.

39. R. Ishizuka and F. Hirata, *Chem. Phys. Lett.*, 2006. **420**: p. 135.

40. D.H. Rank, R.E.K., D.W.E. Axford, *J. Chem. Phys.* , 1949. **17**: p. 1354.

41. W. L. Jorgensen, *J. Am. Chem. Soc.* , 1981. **103**: p. 677.

42. S. Woutersen, U. Emmerichs, and H. J. Bakker, *Science*, 1997. **278**: p. 658.

43. Erik T. J. Nibbering and Thomas Elsaesser, *Chem. Rev.* , 2004. **104**: p. 1887.

44. Zhaohui Wang, Yoonsoo Pang, and Dana D. Dlott, *J. Phys. Chem. A*, 2007. **111**: p. 3196.

45. J.E.Bertie and Z. Lan, *Appl. Spectrosc.*, 1996. **50**: p. 1047.

46. M. L. Cowan, et al., *Nature*, 2005. **434**: p. 199.

47. Quan Li, Tao Li, and Jinguang Wu, *J. Phys. Chem B*, 2000. **104**: p. 9011.

48. Nancy E. Levinger, *Science*, 2002. **298**: p. 1722.

49. J. C. Deàk, et al., *Science* 2004. **406**: p. 473.

50. H. S. Tan, et al., *Phys. Rev. Lett.* , 2005. **94**: p. 057405.

51. J. Faeder and B. M. Ladanyi, *J. Phys. Chem. B*, 2000. **104**: p. 1033.

52. Sanjib Senapati, et al., *Langmuir*, 2002. **18**: p. 7371.

53. Stéphane Abel, et al., *J. Phys. Chem. B*, 2004. **108**: p. 19458.

54. T. Kinugasa, et al., *Colloids Surf. A*, 2002. **204**: p. 193.

55. T. Steinel, et al., *J. Phys. Chem. A*, 2004. **108** p. 10957.

56. A. Rahman and F. H. Stillinger, *J. Chem. Phys.* , 1971. **55**: p. 3336.

57. R. Laenen, C. Rauscher, and A. Laubereau, *J. Phys. Chem. B*, 1998. **102**: p. 9304

58. R. Laenen, C. Rauscher, and A. Laubereau, *Phys. Rev. Lett.* , 1998. **80**: p. 2622.

59. S. Mukamel, *Principles of Nonlinear Optical Spectroscopy, Oxford University Press, New York*, 1995.

60. Giuseppe Onori and Ado Santucci, *The Journal of Physical Chemistry*, 1993. **97**: p. 5430.

61. Nathaniel V. Nucci and Jane M. Vanderkooi, *J. Phys. Chem. B*, 2005. **109**: p. 18301.

62. Dean S. Venables, Kathie Huang, and Charles A. Schmuttenmaer, *J. Phys. Chem. B*, 2001. **105**: p. 9132.

63. Ivan R. Piletic, et al., *J. Phys. Chem. A*, **110**, 4985 (2006), 2006. **110**: p. 4985.

64. W. F. Murphy, *J. Chem. Phys.* , 1977. **67**: p. 5877.

65. S. A. Clough, et al., *J. Chem. Phys.*, 1973. **59**: p. 2254.